Final Report

Date of Report: *December 31, 2015*

Contract Number: *DTPH56-13-H-CAAP04*

Prepared for: *James Merritt, DOT-PHMSA*

Project Title: *Proactive and Hybrid Sensing Based Inline Pipeline Defects Diagnosis and Prognosis*

Prepared by: *University of Colorado-Denver, Arizona State University*

Contact Information: *Xiaoye (Mia) Chen, Xiaodong Shi, Deepak Kumar, Sahi Jain, Laura Spellman, Dr. Yiming Deng, Dr. Yongming Liu*

Project ending date: *December 31, 2015*

ABSTRACT

Pipeline infrastructure and its safety is critical for the recovering of U.S. economy and our standard of living. Failure inevitably occurs in plastic piping materials and impingement failure is caused by high localized stress concentration combined with defects and inclusions. As emerging plastic materials are increasingly used for pipelines, new sensing techniques are required to diagnose and prognoses damage and imperfections early and before they become failure critical. The object of this project is to develop a near-field microwave microscopic (NFMM) imaging method to identify and characterize many types of injurious pipe body proactively with superior resolution and high sensitivity. This work resulted in an information framework integrating the residual strength calculation, uncertainty quantification and propagation analysis using a Bayesian updating process to advance pipeline reliability evaluation and risk assessment tool.

TABLE OF CONTENTS

LIST OF FIGURES……6
LIST OF TABLES……12
CHAPTER 1 INTRODUCTION 10
CHAPTER 2 SCANNING PROBE DEVELOPMENT 11
2.1. Resonant Slit Scanning Probe Development 11
2.2. Co-axial Tip Antenna (CTA) Sensor Development 12
2.3. Copper-SMA Probe Tip Development 15
2.3.1. DC Signal Amplifier Circuit Development 17
2.3.2. Data Acquisition Speed Optimization using NI DAQ Card 18
2.3.3. Sparse Sampling and Estimation for Microwave Near Field Imaging 20
2.4. Multi - Channel Sensor 23
CHAPTER 3 PHASE IMAGING APPROACH 25
3.1. Phase Extraction for the Proposed Hybrid Pipe Imaging 25
3.1.1. HP8559A Phase Measurement Simulation 26
3.2. Phase Information Acquisition Approaches 28
3.2.1. Background 28
3.2.2. Pre-Requisite Information 28
3.2.3. Analog Mixing 28
3.2.4. Mathematical Model 28
3.2.5. Analytical Analog Mixing Approach 29
3.2.6. Numerical MATLAB Mixer Method 30
3.2.7. LTSPICE Double Balanced Diode Ring Mixer 31
3.2.8. Phase Detection using SM1717 Mixer 32
3.3. Phase Detection System Prototyping for Piping Materials Characterization 34
CHAPTER 4 PARAMETRIC STUDY FOR NEAR FIELD MICROWAVE IMAGING SIMULATION 40
4.1. FEKO Simulation for Single Channel Sensor 40
4.2. FEKO Simulation for Multi - Channel Sensor 41
4.3. HFSS Simulation for Single Channel Sensor 43
CHAPTER 5 BACKGROUND AND INTRODUCTION 49

CHAPTER 6 NUMERICAL SIMULATION USING EXTENDED FINITE ELEMENT METHOD(XFEM) AND COHESIVE ZONE METHOD(CZM)..... 53

6.1. Overview and Objective 53

6.2. Impingement failure simulation under static loading 54

6.3. Impingement failure simulation under static loading 58

6.4. Slow crack growth due to creep and impingement loading..... 60

CHAPTER 7 PROBABILISTIC PROGNOSIS ANALYSIS..... 69

7.1. Overview and Objective 69

7.2. Design of Experiments and Surrogate Model Development 69

7.3. Uncertainties Reduction using Bayesian Updateing..... 73

CHAPTER 8 EDUCATIONAL ACHIEVEMENTS 77

REFERENCES CITED..... 80

LIST OF FIGURES

Figure 2.1 Narrow Resonant Slit (NRS), with 45 degrees and 0 degree polarization, respectively. *11*
Figure 2.2 Testing results on calibration sample using NRS probe. *12*
Figure 2.3 Experiment setup with CTA sensor: (a) sensor tip and (b) signal spliter and amplification. *13*
Figure 2.4 Comparision between imaging results obtained by (a) cm-scale open ended WG, (b) mm-scale NRS and (c) mm-scale CTA probes. *13*
Figure 2.5 . Damage imaging demonstrated using CTA (from (a) to (c)): HDPE pipe, GFRP, Aluminum materials *14*
Figure 2.6 Copper-SMA probe tips with various diameters and lengths *15*
Figure 2.7 S11 signal for 3GHz copper-SMA probe tip on VNA. *16*
Figure 2.8 Scan result comparison between copper-SMA probe tip (a) and CTA tip (b) *17*
Figure 2.9 Circuit schematic for DC signal Amplifier *17*
Figure 2.10 National Instruments PCIe 6341 card and BNC 2110 Adapter for optimized DAQ module *19*
Figure 2.11 Scan result obtained using NI PCIe and DMM approaches: (a) Results with large FOV and (b) Results with smaller FOV. *19*
Figure 2.12 (a) Fourier Transform. (b) DCT Transform *20*
Figure 2.13 Vertical skipping of lines by 90% and recovered signal *21*
Figure 2.14 Horizontal skipping of lines by 34% and recovered signal *21*
Figure 2.15 Recovery from 2% randomly sampled data set *21*

Figure 2.16 Demonstration of the CS-based reconstruction which a small portion of the raster scanning region was covered. The same mechanism will be tested for in-field pipe imaging 23
Figure 2.17 Linear array prototype 23
Figure 2.18 Design comparison of control circuit and current experiment setup 23
Figure 2.19 Control Circuit Design 24
Figure 3.1 NFMWI Phase Measurement Simulation: Rx Signal (right); Scalar Spectrum Analyzer Measurement (left) 26
Figure 3.2 NFMWI Phase Measurement Simulation: 90 degrees Phase Shift Rx Signal (left); Scalar Spectrum Analyzer Measurement (right) 27
Figure 3.3 Output Signal Power Displayed on the Function Generator 27
Figure 3.4 Illustration of phase detection methodology through complex demodulation approach. 29
Figure 3.5 The output is double frequency at 20 GHz floating around a DC value. 30
Figure 3.6 Phase diff. between signals varied 0 to 180 deg. in 9 deg. intervals. 31
Figure 3.7 (a) Double Balanced Diode Ring Mixer Schematic and (b) the output is double frequency at 20 GHz. 32
Figure 3.8 IF voltage measured at each phase diff. increment from 0 deg. To 180 deg. 32
Figure 3.9 Experimental IF voltage measurement schematic. 33
Figure 3.10 IF voltage measured at each phase diff. increment from 0 deg. to 180 deg. 34
Figure 3.11 LEAP NFMWI Phase Detection block diagram and hardware setup 35
Figure 3.12 Mid-size Triangle of Al calibration sample 35
Figure 3.13 (a) Image of Mixer IF voltage measurements and (b) corresponding image of Phase Differences after post-processing. 36
Figure 3.14 Resulting image of the entire calibration sample: (a) image of Mixer IF voltage measurements and (b) corresponding image of Phase Differences after post-processing. 36

Figure 3.15 Resulting image of the entire calibration sample after parameters optimization: (a) image of Mixer IF voltage measurements and (b) corresponding image of Phase Differences after post-processing. 37
Figure 3.16 Phase map result of a coin hidden under HDPE. (a) HDPE sample (b) HDPE sample with coin (c) Scanning results 38
Figure 3.17 Phase scan result for CFRP.(a) Carbon Fiber Reinforced Polymer sample. (b) Phase scan result 38
Figure 3.18 Phase scan result for 3D plastic printing sample.(a) 3D plastic printing sample. (b) Phase scan result 39
Figure 3.19 . Scan result of calibration sample with 6 holes.(a) Calibration sample with 6 holes. (b) Phase scan result 39
Figure 4.1 Simulation model with different SUT geometry: (a) PEC material with a through circle at the center. (b) homogeneous PEC material 40
Figure 4.2 Simulated electric field intensities along x direction of scanning 41
Figure 4.3 Geometry of a flat surface multi channel scanner 42
Figure 4.4 Near field of each antenna of flat surface multi channel scanner 42
Figure 4.5 Simulation model for 12 channel NFMW sensor.(a) Geometry of design. (b) Near field 43
Figure 4.6 Simulation model for single monopole antenna.(a) Geometry of design. (b) Near field radiation pattern. (c) Reflection coefficient of antenna 44
Figure 4.7 Near field of flat surface multi channel scanner (a) Geometry of the sensor array on a flat surface. (b) Near field magnitude result of the sensor array. (c) Reflection coefficient of each antennas 46
Figure 4.8 Near field of cubic shape multi-channel NFMM scanner (a) Geometry of the cubic shape sensor array. (b) Near field magnitude of the sensor array. (c) Reflection coefficient of each antennas. (d) Radiation pattern of the sensor array 48
Figure 5.1 Ductile Failure Resulting From a Quick Burst Test[1] 50
Figure 5.2 SCG Failure Morphology [1] 50

Figure 5.3 RCP rupture induced in a Small-Scale Steady State S-4 test [1] 51
Figure 5.4 Rock impingement 51
Figure 5.5 Force fracture of joints 51
Figure 5.6 Improper squeezing 52
Figure 5.7 Welding location leaking 52
Figure 6.1 Schematic illustration of the traction separation law in CZM 53
Figure 6.2 Geometry and meshing of the pipe model 55
Figure 6.3 Crack Propagation 56
Figure 6.4 Von – mises Stress Plots 57
Figure 6.5 Parametric study for static failure due to impingement 58
Figure 6.6 Geometry and meshing of the T joint 59
Figure 6.7 Simulated force fracture at a T joint 59
Figure 6.8 Schematic illustration of creep behavior [11] 61
Figure 6.9 Schematic illustration of strain recovery [11] 61
Figure 6.10 Typical tensile stress-strain curves for several materials [9] 62
Figure 6.11 Creep response of a propylene-ethylene copolymer at 20 °C [9] 63
Figure 6.12 Simulation results at different time steps 64
Figure 6.13 Model setup for notched plate model 65
Figure 6.14 Simulation results at different time step 65
Figure 6.15 Model for the creep analysis 66
Figure 6.16 Mesh near the impingement location at the outer and inner surfaces 67
Figure 6.17 Simulation results of slow crack propagation 68
Figure 7.1 The project of 20 samples on each 2D plane 70
Figure 7.2 The crack growth curves for 8 DoEs 71
Figure 7.3 The comparison between true and predicted crack length 72
Figure 7.4 The crack length variation for the perturbation of each design variable 73
Figure 7.5 The prior belief of the crack growth curve 75

Figure 7.6 The updated crack growth curves (a), Updating 1. (b), Updating 2. (c), Updating 3. (d), Updating 4..... *76*
Figure 7.7 The posterior distribution of principal stress and applied load *76*

LIST OF TABLES

Table 3.1 Specifications for the SM1717 Mixer..... *33*
Table 7.1 Sampling interval for each random variable..... *70*
Table 7.2 The 20 DoE samples generated using LHS *71*
Table 7.3 Prior distribution of these five design variables..... *75*

CHAPTER 1 INTRODUCTION

As emerging plastic materials are increasingly used for pipelines, new sensing techniques are required to diagnose and prognoses damage and imperfections early and before they become failure critical. The team identified a number of damage types that would affect these pipelines, including rock impingement induced cracking, force fracture of joints, improper squeezing induced failure, welding location leaking, and crack propagation. This project developed a near-field microwave microscopic (NFMM) imaging method to identify and characterize these and other types of injurious pipe body proactively with superior resolution and high sensitivity.

NFMM is a nondestructive, low power, and low cost method of imaging. It can be used with a contact and noncontact probe and provides high contrast and high spatial resolution. It is used to characterize materials, behaviors, and microstructures.

The group began testing on an aluminum calibration sample, as well as a concrete sample, and later progressed to several types of plastics, including polyamide-6 (PA-6), carbon-fiber reinforced polymer (CFRP), High-density polyethylene pipe (HDPE), polyethylene (PE), and glass fiber reinforced polymer (GFRP).

Chapter 2 introduces the different types of scanning sensors that have been developed in the group. Phase scan methods are discussed in Chapter 3. Chapter 4 presents the parametric study for different types of multi-channel sensors. Chapter 5 gives the background of numerical modeling of piping materials damage followed by the simulations results in Chapter 6. Chapter 7 introduces the probabilistic prognosis analysis methodology and presents the results and discussion that combines contributions from both CU and ASU. Chapter 8 summarizes the significant research and educational impacts of the CAAP funding to the trainees and students at both research institutes.

CHAPTER 2 SCANNING PROBE DEVELOPMENT

2.1. Resonant Slit Scanning Probe Development

CAAP research group at CU continues the innovative sensing system development and initially adopted an open ended waveguide geometry as the scanning probe to obtain C-scan images in March, 2014. Even though the sensing results are consistency, the resolutions in both x- and y- directions are not satisfactory (tens of millimeters) for the proposed applications. Since the resolution of NFMW imagres are primarily base on the size of the probe, the smaller size of the probe we are using, the better resolution we can get for the scanning results. By putting a slit at the end of the broadwall coupler waveguide, will help reduce the size of the probe to get the better scanning resolution. Starting April, 2014, CU team designed a narrow resonant slit to reduce the size of NFMW pipeline transducer. Two slits with different source polarization directions are shown in Figure 2.1.

Figure 2.1 Narrow Resonant Slit (NRS), with 45 degrees and 0 degree polarization, respectively.

The dimension of the above NRS geometry is given by:

$$\frac{a}{b}\sqrt{1-\left(\frac{\lambda}{2a}\right)^2}=\frac{a'}{b'}\sqrt{1-\left(\frac{\lambda}{2a'}\right)^2} \tag{2.1}$$

The frequency of the microwave signal is 10 GHz, therefore the radiation wavelength λ, is 3 cm. The dimension of the broadwall coupler waveguide is a-by-b, where a = 2.2 cm, and b = 1 cm. From equation (2.1) above, the dimension of the slit will be as follows: a' = 1.5cm, b' = 0.8mm. This improved design will help reduce the size of the scanning probe and also help with impedance matching before and after the slit by reducing the reflection

from the surface of the sample under test (SUT). Figure. 2.2 shows the calibration sample, with cutouts of various size and shapes, as well as the results from the NRS probe scan. Each shape can be identified, showing the improved spatial resolution to millimeter scale, although severe artifacts and skew effect were observed. It is possible to remove his with post-processing techniques.

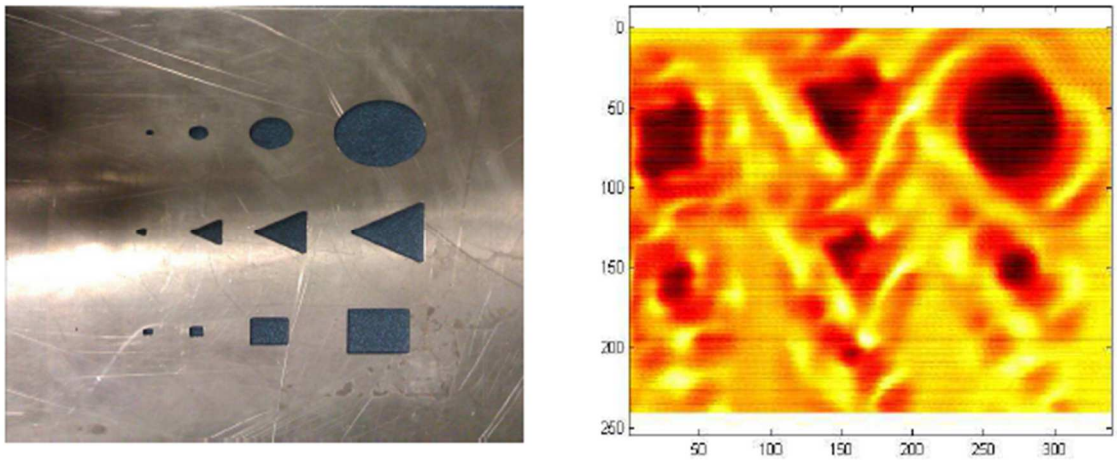

Figure 2.2 Testing results on calibration sample using NRS probe.

2.2. Co-axial Tip Antenna (CTA) Sensor Development

In the first quarter of development, The CU Team proposed the use of a coaxial tip antenna (CTA) to further improve the spatial resolution of the scan. The diameter of the inner conductor of the coaxial cable is 1.02 mm, which is the smallest probe proposed. The length of antenna was designed to be half of the wavelength (1.5 cm) of the signal to have the maximum return loss for the antenna, and to have higher directivity. One end of the coaxial cable was trimmed to expose 1.5 cm of the inner conductor for use as the CTA antenna. This design has great advantages, as it is low cost and easy to fabricate. In Figure 2.3 below, the experiment setup is pictured. The signal from the microwave generator was transmitted into a coupler, which reduced the noise generated by the broadwall coupler waveguide.

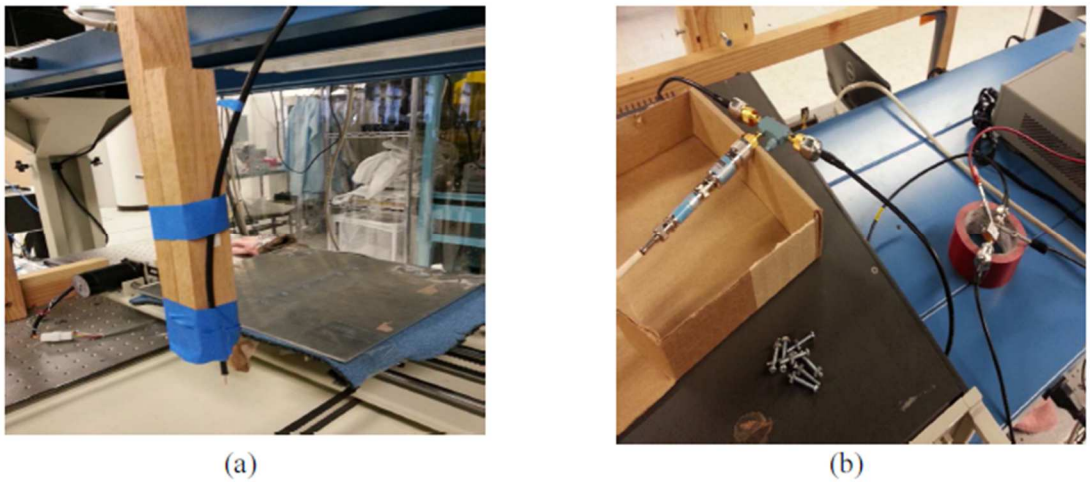

Figure 2.3 Experiment setup with CTA sensor: (a) sensor tip and (b) signal spliter and amplification.

The CU team demonstrated that the SMA connector performed better at high frequency, was able to lower the noise between connectors further. Figure 2.4 shows the comparison of the calibration scanning results among different probe tips: cm-scale open ended WG, mm-scale NRS probe and mm-scale CTA probe.

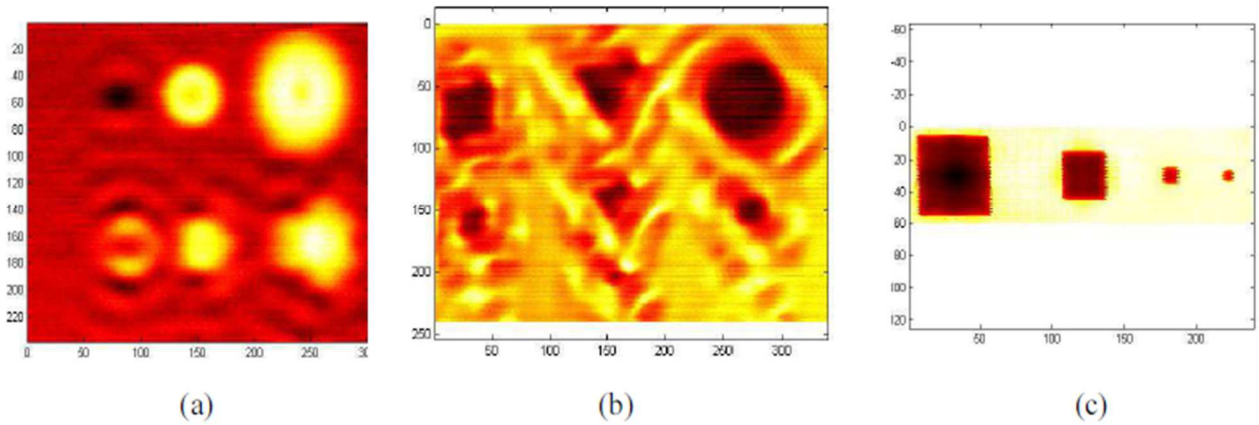

Figure 2.4 Comparision between imaging results obtained by (a) cm-scale open ended WG, (b) mm-scale NRS and (c) mm-scale CTA probes.

Besides calibration sample, CU team also tested the CTA sensor on proposed testing materials. Figure. 2.5 shows the results of different materials.

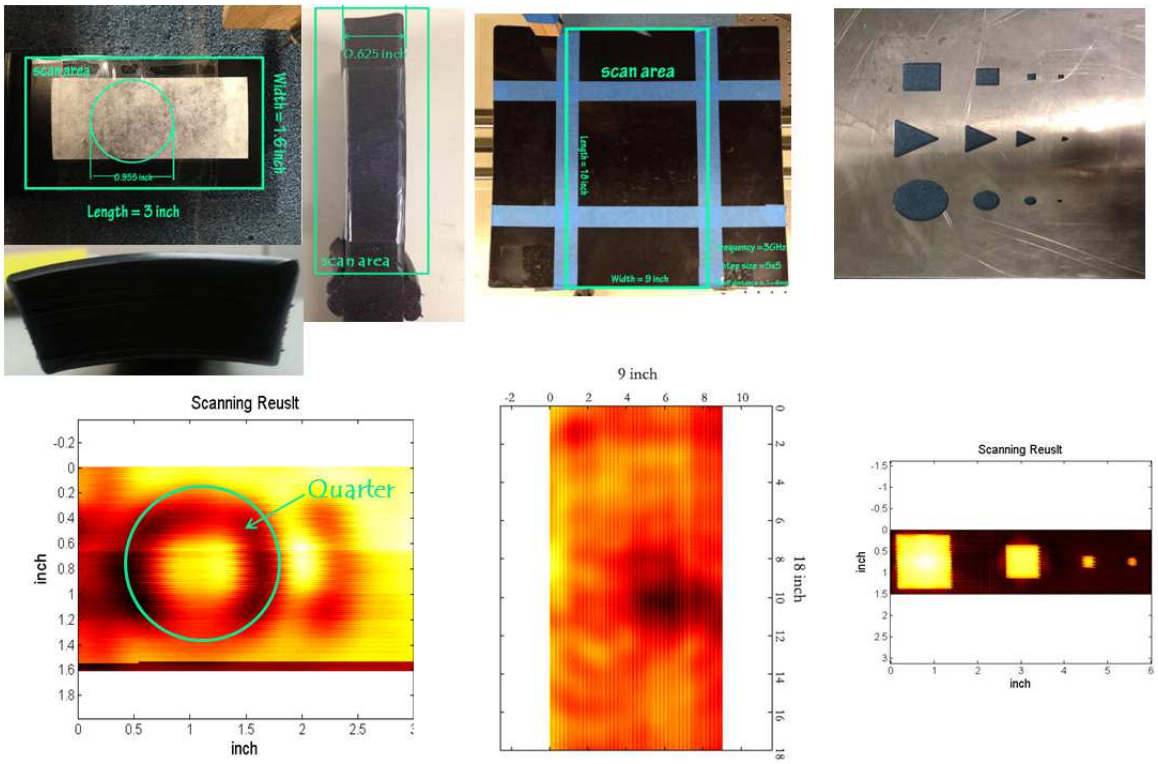

(a) (b) (c)

Figure 2.5 . Damage imaging demonstrated using CTA (from (a) to (c)): HDPE pipe, GFRP, Aluminum materials

HDPE pipe material was tested using the same sensing setupas calibration sample. We put a quarter underneath the sample to test the CTA microwave probe penetration ability beyond skin depth (theoretically less than 1 mm for the sample under test). The scan result shows the quarter can be seen clearly in the image, even for a plastic HDPE pipe with thickness of 0.625 inches. The size of the object can be successfully estimated as shown in Figure. 2.5(a). However, the resolution for the result was not good due to the "shadowing effect" of CTA setting, which is due to its poor point spread function (PSF). Then we did some experiments with GFRP material using a sample size that was 17 x 17 square inches. We did a couple scans for the center rectangular area marked in the figure (Fig. 2.5(b)). For several scanning image results we consistently saw a dark area in the obtained images, which also revealed the inhomogeneous distribution of the material properties inside of GFRP sample. Further imaging methods are needed to confirm the nature of the subsurface damage.

2.3. Copper-SMA Probe Tip Development

Although the CTA geometry was able to obtain better scanning results than other previously tested probe types, the inner conductor of the coaxial cable was not mechanically solid enough to perform a contact scan, giving a “Shadow effect” to the scan results. A copper-SMA probe tip was developed during Quarter 3 to combat this. These probes tip are designed to attach to an SMA connector to implement 2D imaging with good impedance matching. They are also strong enough to be used in a contact scan. Copper probe tips with different diameters and lengths were developed to suit different imaging frequencies and sizing of scanned material. Figure 2.6 shows several copper probe tips developed and fabricated at CU LEAP group.

Figure 2.6 Copper-SMA probe tips with various diameters and lengths

Because of the relation between spatial resolution and probe tip size, The diameters manufactured were 4mm, 3mm and 2mm, respectively, and the lengths were developed to scan at 3 GHz and 10 GHz frequencies. In order to have higher directivity, we designed the length the of antenna to be ½ of the radiation wavelength corresponding to the 3 GHz and 10 GHz scan frequencies to minimize the return loss for the antenna. Figure 2.7 is the S11 signal for 3 GHz copper-SMA probe tip on the Vector Network Analyzer, characterized at CU-LEAP. We expected to see the strength of the return signal dip at 3 GHz, which means the signal was transmitted effectively from the tip to the piping materials at 3GHz as it was designed.

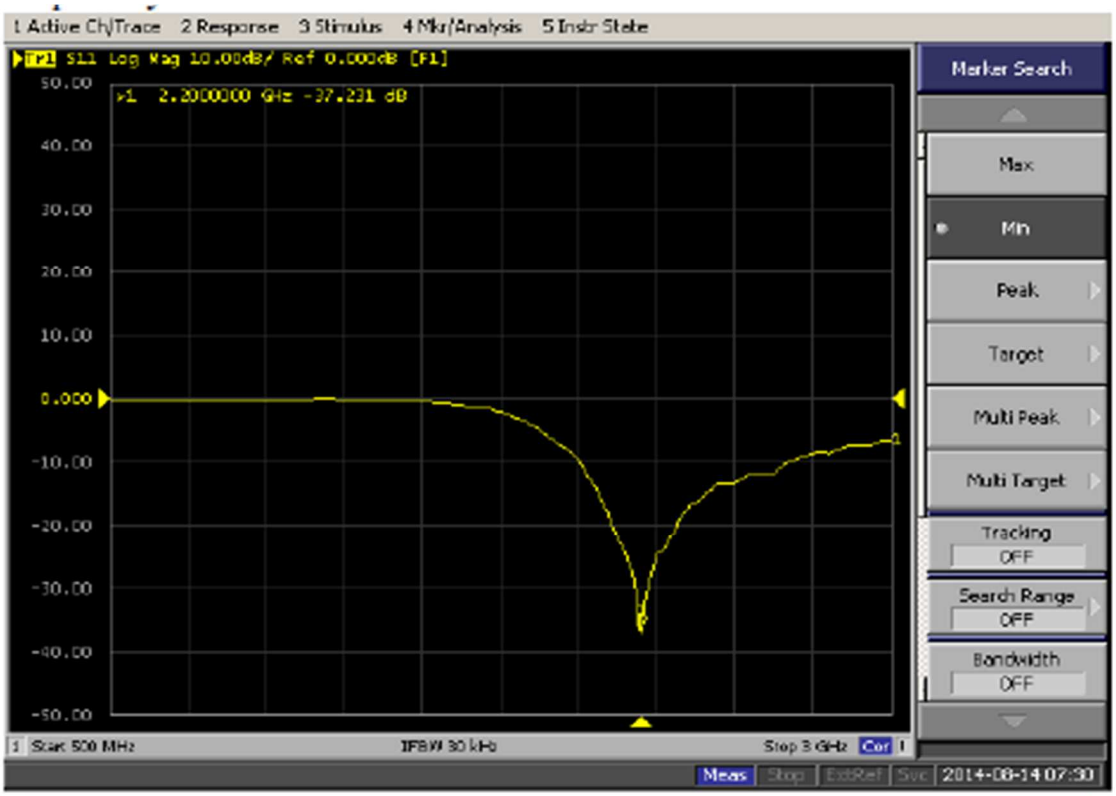

Figure 2.7 S11 signal for 3GHz copper-SMA probe tip on VNA.

However, the S11 curve actually indicated that the signal was mostly transmitted at 2.2 GHz. This means the probe tip we designed is able to transmit and receive near-field microwave signals, but not at the exact frequency we expected. Although clearer and higher resolution images were obtained using the new probes, further investigation was needed to explain the frequency shift issue.

To improve the imaging quality, the CU team put a ground plate at the bottom of the tip to reduce the noise level that was initially observed during trial scans. Since SMA connectors work better than most other types at high frequencies, SMA cables were used as transmission lines to transfer the signals, instead of the coaxial cables in CTA setup. The results shown in Figure 2.8 clearly depict the shapes of the calibration sample and also reduce the “shadow effect” around the defects, The copper-SMA probe tip is able to give a sharper image compared to other proposed probes.

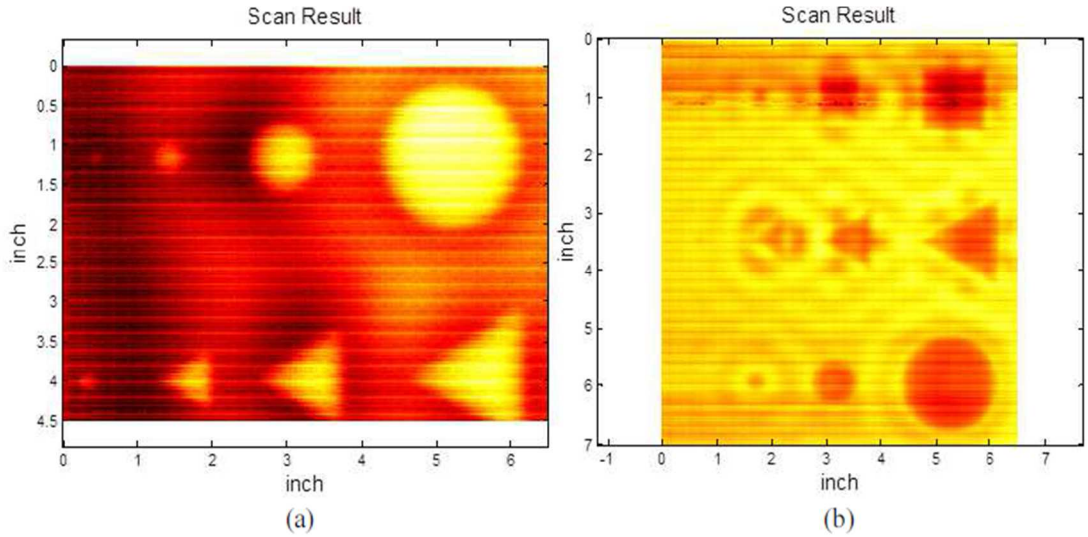

Figure 2.8 Scan result comparison between copper-SMA probe tip (a) and CTA tip (b)

2.3.1. DC Signal Amplifier Circuit Development

Having a stronger return signal has always been our goal for the project. CU CAAP team designed a DC amplifier to accomplish this goal in Quarter 3. Figure 2.9 shows the three op-amp-circuit schematic used to amplify the return signal designed by CU LEAP.

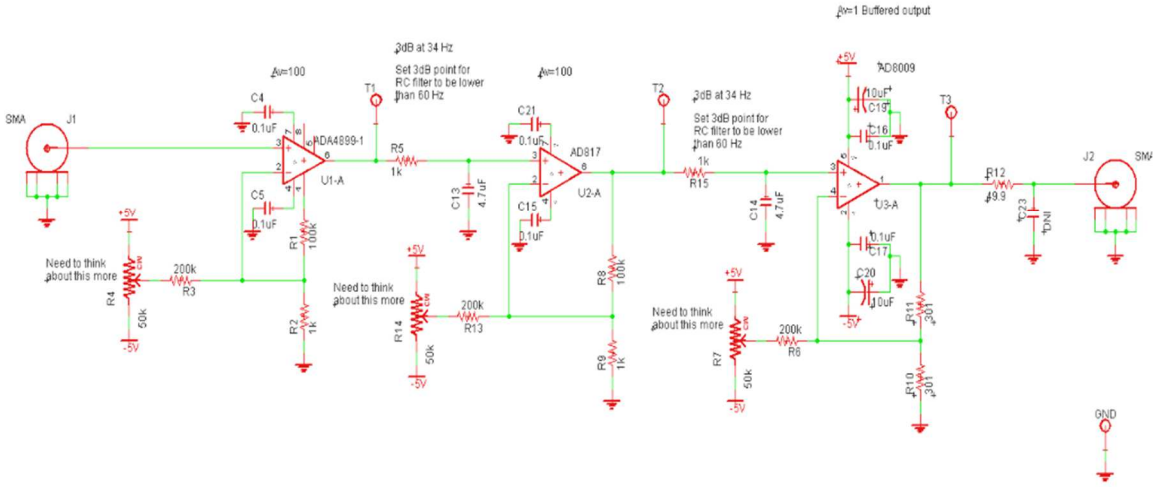

Figure 2.9 Circuit schematic for DC signal Amplifier

We used ADA4899, AD817 and AD8009 op-amps in the design for this CAAP project. The first and second stages are able to amplify signal by as much as 100 times each. Thus

the circuit was designed to amplify the signal up to 10000 times. Each stage also has an adjustable resistor to increase the signal to noise ratio. Since the return signal measured from the scan system is in the millivolts range, this amplifier will help improve the image quality. The input voltage can range from 6V to 12V.

2.3.2. Data Acquisition Speed Optimization using NI DAQ Card

With the support of this grant and another MPP grant from CU, a high sampling speed data acquisition A/D card was obtained, manufactured by National Instruments. Increasing the speed of imaging and data processing speed is always critical for the piping material losses and defects diagnosis. In the 4th quarter, we successfully increased the speed of imaging using NI PCIe 6341 module. Before this quarter, we use DMM (Digital Multimeter) to receive the converted DC signals, which are the reflected signals from SUT and proportional to the electric field intensities. In our previous effort, the 2D scanner always had to wait for DMM to receive the data before moving to the next step to make sure the data point to the right location, this will cause significant delay for every single step. Since the sampling rate of DMM is only 70 samples per second, the scanner cannot move fast due to this bottleneck. The NI PCIe 6341 has a sampling rate up to 500K samples per second, which can increase the scanning speed dramatically, and also able to averaging data at almost real time. We conducted multiple testing and concluded that the speed of scanner has been improved at least three times faster comparing to previous efforts without scarifying the resolution of acquired images. Figure 2.10 shows the photos of the NI PCIe 6341 and BNC 2110 DAQ module used for this project.

Figure 2.10 National Instruments PCIe 6341 card and BNC 2110 Adapter for optimized DAQ module

Figure 2.11 shows the scanning result that generated from NI PCIe and DMM in (a) and (b), respectively. Figure 2.11(a) is the data collected using NI PCIe 6314 while Figure 2.11(b) is collected using DMM approach. The two results show distinct shapes of the calibration sample with good spatial resolutions, however Figure 2.11(a) was generated in a much shorter time than Figure 2.11(b) even with more scanning area was covered. To further improve the scanning speed for this CAAP project, some other different methods have been discussed in the LEAP group, such as compressive sensing and image reconstruction algorithms after all the measurement data were acquired.

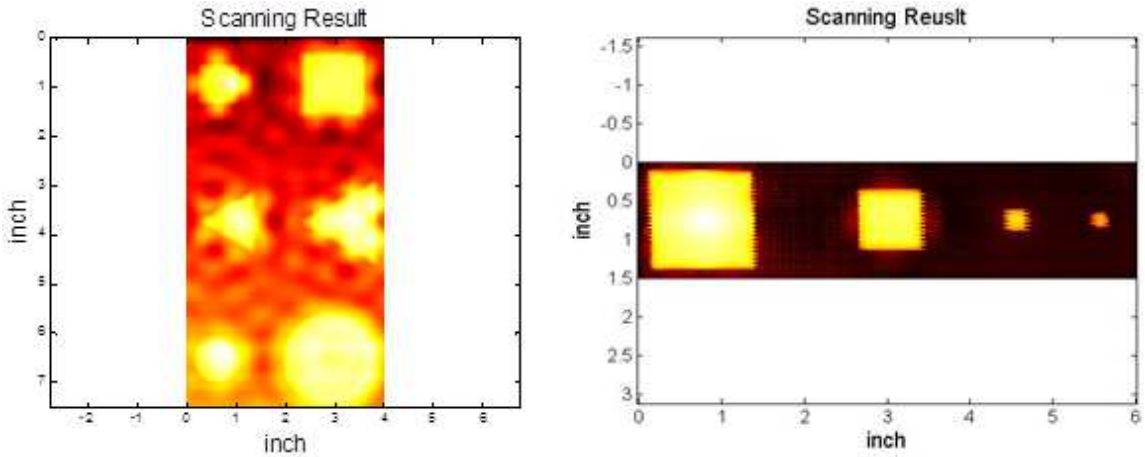

(a) (b)

Figure 2.11 Scan result obtained using NI PCIe and DMM approaches: (a) Results with large FOV and (b) Results with smaller FOV.

2.3.3. Sparse Sampling and Estimation for Microwave Near Field Imaging

Every imaging modality developed in this world have one common goal to extract meaningful information about object. Sensing and estimation are the two principal steps to reach the final outcome of the imaging techniques. In our experiment, large amount of NFMM data are collected to form an image for further investigation. Due to the experiment design, there are several difficulties when come to collecting data, such as incorrectly synchronizing with imaging speed, storing capabilities, transmission bandwidth and processing efficiently. The goal for this study is to have meaningful information by taking fewer samples.

There are several sparse estimation techniques, such as Fourier transform technique, DCT transform technique and K-SVD dictionary learning algorithm. Figure 2.12 shows the Fourier and DCT transform of the original signal.

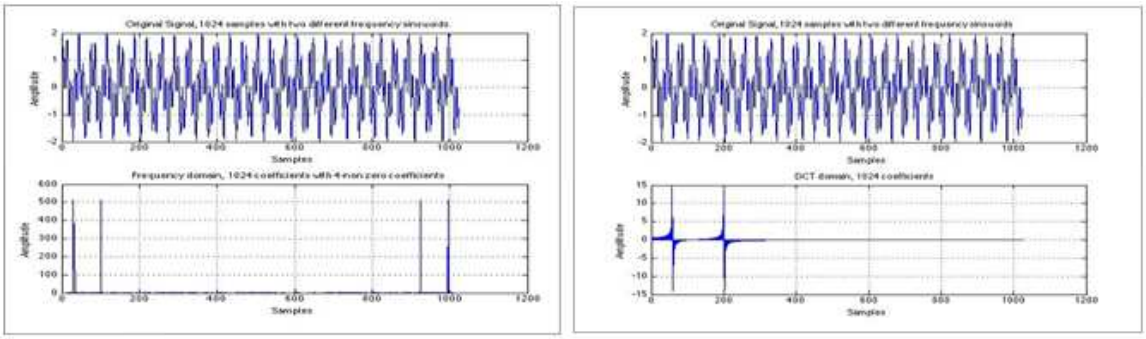

(a) (b)

Figure 2.12 (a) Fourier Transform. (b) DCT Transform

Sparse sampling and estimation comes to the real application over microwave imaging. Implementation starts with simulating codes with complete set of raw data. We scanned 100% aluminum sample and save the raw data. Simulation starts with loosing 36%, 90%, 99% and try to estimate original data set. Figure 2.13- Figure 2.15 gave us promising results while using less sample to recover the original signals. Which can help us reduce the scanning time in the future.

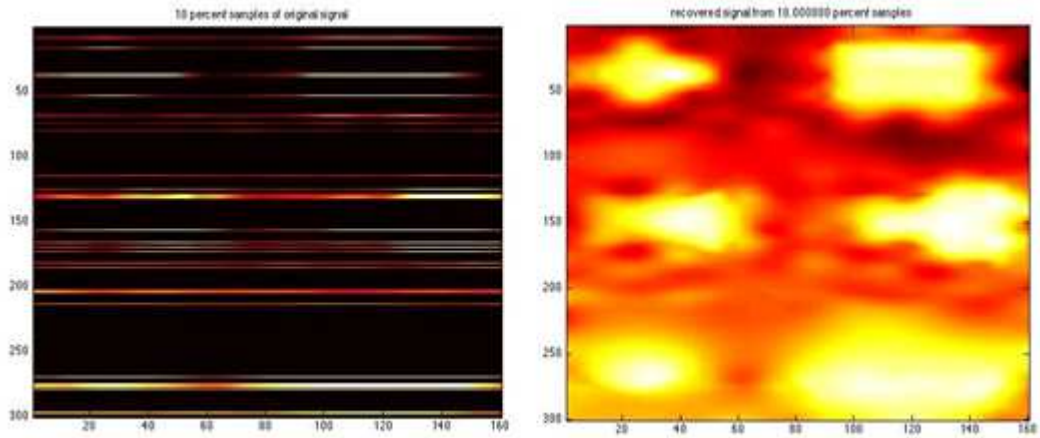

Figure 2.13 Vertical skipping of lines by 90% and recovered signal

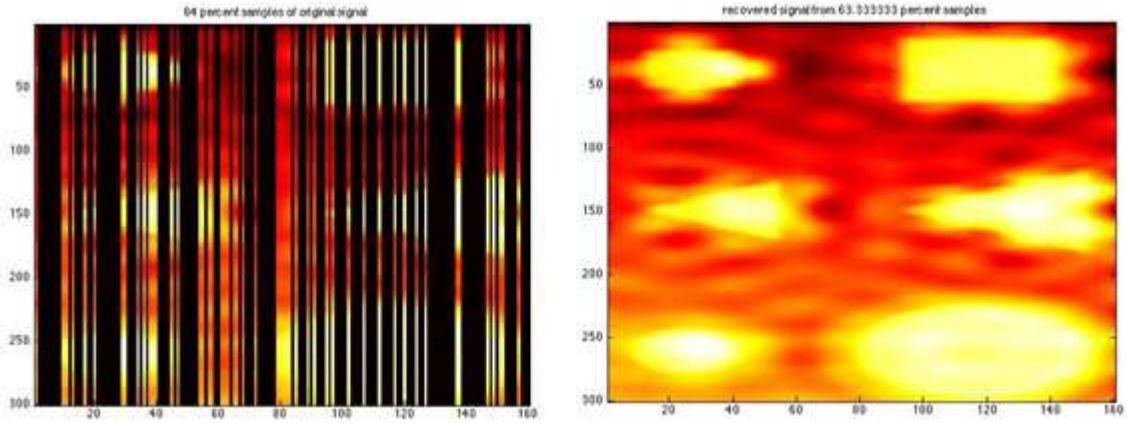

Figure 2.14 Horizontal skipping of lines by 34% and recovered signal

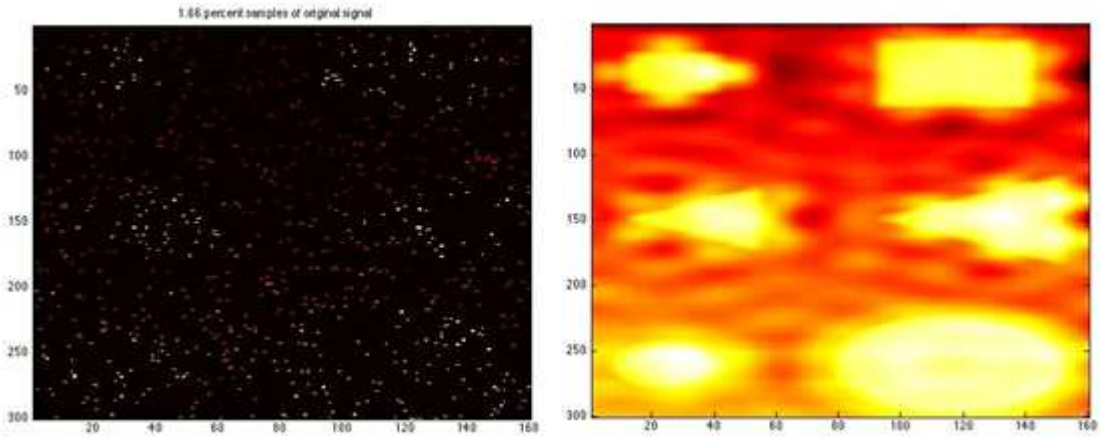

Figure 2.15 Recovery from 2% randomly sampled data set.

We also did the experiment about reducing the scanning area to try to recover the whole target to test the compressive sensing technique. Figure 2.16 shows the results of the experiment. Figure 2.16(a) is the scanning result from the scan by skipping 50% of the Horizontal lines and shows a good recovery. Figure 2.16(b) is the scanning result of aluminum sample with multiple rings by skipping 50% of samples, scanning result are also recovered. Even though the recovery is good, there are still information missing from the recovery image. It because of the raster scanning platform and the stepper motors are not synchronized when skipping rows or columns start. This due to the stepper motors are not moving at a constant speed.

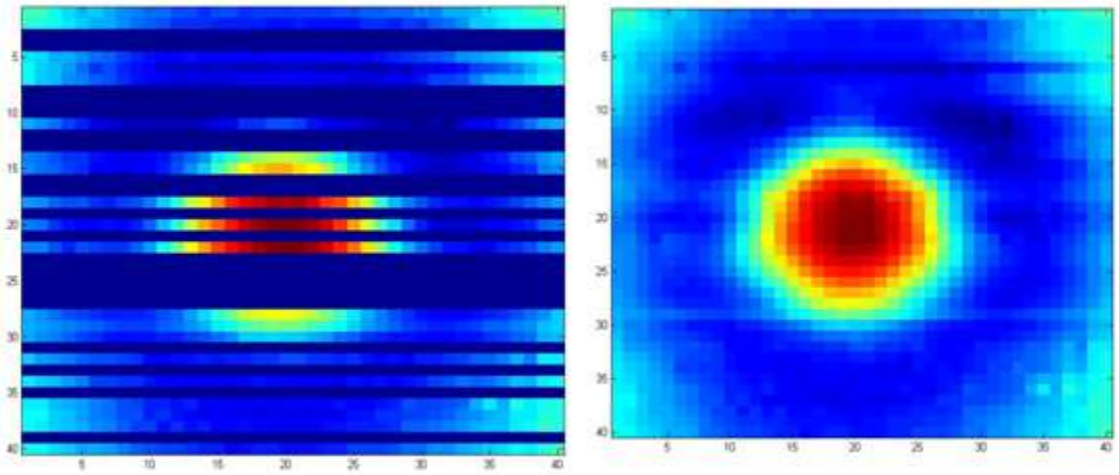

(a)

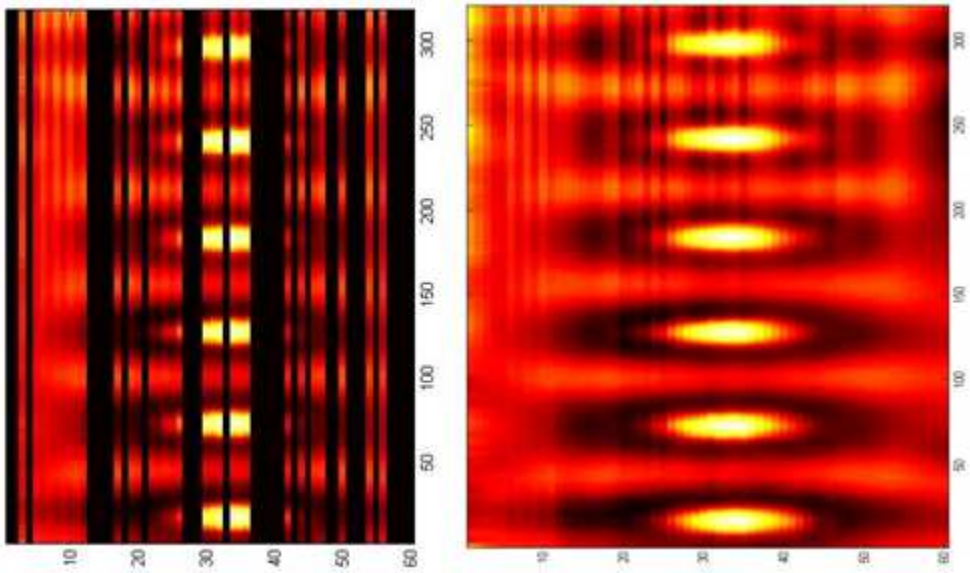

(b)

Figure 2.16 Demonstration of the CS-based reconstruction which a small portion of the raster scanning region was covered. The same mechanism will be tested for in-field pipe imaging

2.4. Multi - Channel Sensor

LEAP has designed and fabricated the multi-channel scanning sensor tip for better scanning efficiency and make the proposed technique more practical and relevant to industry, the first experiment prototype is shown in Figure 2.17.

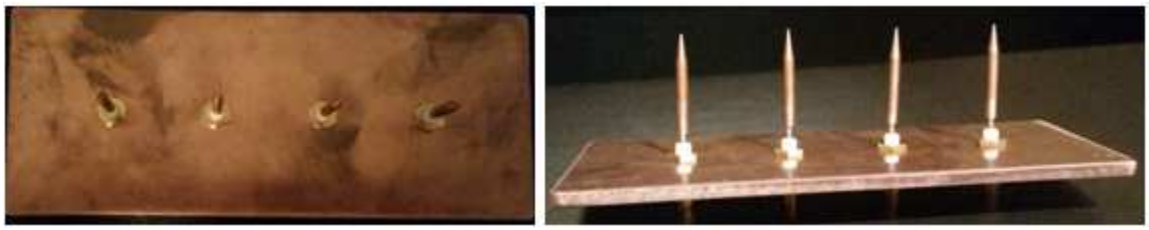

Figure 2.17 Linear array prototype

A control circuit for the multi-channel scanning sensor has also been designed. The control circuit was designed to have the same setup as the current experiment. The innovative design of the control circuit shows in Figure 2.18(a). Compared with the current experiment, shown in Figure 2.18(b), the control circuit compresses the directional coupler, RF to AC converter and data collection together to perform the same function. The control circuit uses a microcontroller to control the input and receive signal. There is no connection between data processing and receiving signal in the control circuit design, which will reduce the scanning time.

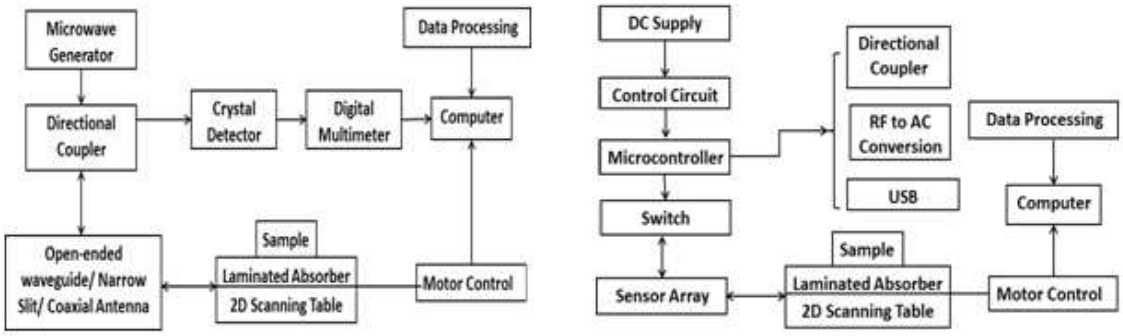

(a) Improved design with Control circuit (b) Current experiment design

Figure 2.18 Design comparison of control circuit and current experiment setup

The control circuit schematic is shown in Figure 2.19. We had several difficulties while designing the control circuit. First is how to split the signal equally to each channel. This is important to the experiment to make sure the signal level is equal. We planned to use PCB trace to build the splitter. Since the operation frequency of the scanning sensor is at 3GHz, it is difficult to avoid the noise if we have long traces on PCB. Instead of building a splitter, we chose to use a high speed switch to control the signal. The switch will allow the signal transfer to each probe sequentially. This will avoid the noise generated between the traces, also help avoid the noise that generate between the probes. The second problem we encountered during the design was how to store the return signal data. The goal of the design is for the field testing in the future. How to effectively store the data is important. Instead of using NI DAQ card as we do in our experiment, we chose to use a USB port for storing data for later processing. This will allow the design to be portable for future field testing. The USB port will also help reduce the scanning time since there is no data processing involved. The last question we had during the design process is how to generate the maximized input the signal. Even though the scanning sensors are designed for 3GHz signal, there will be slightly difference between each probe due to the machine error. To be able to adjust the frequency to maximize the signal would be another requirement for the control circuit. We chose Voltage Control Oscillator (VCO) to control the input signal. This will give us the freedom to adjust the input signal to obtain the better resolution.

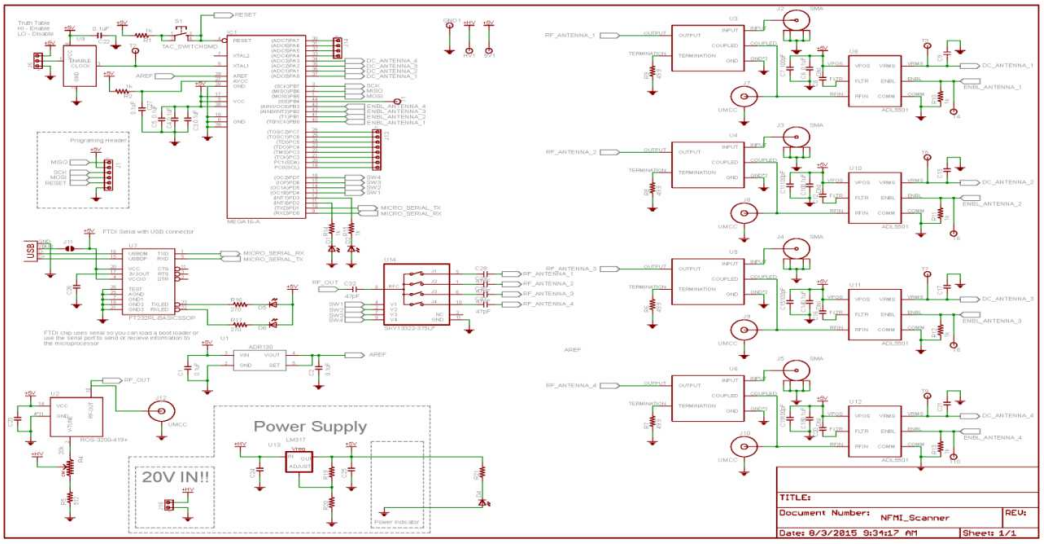

Figure 2.19 Control Circuit Design

CHAPTER 3 PHASE IMAGING APPROACH

3.1. Phase Extraction for the Proposed Hybrid Pipe Imaging

CU CAAP team has developed an approach to measure phase difference between the transmitted (Tx) and received (Rx) signals of the Near-Field Microwave Imaging system to see if plotting phase difference improves resolution. The difference in phase between transmitted signal (Tx) and the reflected signal (Rx) is a fruitful area for research and investigation besides magnitude information that is been collected from the sample under test. Here we are collection phase information from reflected signal at 10 GHz to study the characteristics of plastic and composite piping materials. These plastic and composites are being recently used in the industry to replace old materials for their limitations like age and heavy weight.

It was thought the phase difference between the transmitted signal, Tx, and received signal, Rx, in the LEAP Near-Field Microwave Imaging System (NFMWI) could be acquired using a HP8559A spectrum analyzer. This is not possible because the HP559A is a scalar spectrum analyzer. Scalar spectrum analyzers only measure and report the amplitude vs. frequency of the input signals over a specified frequency span. In the NFMWI system the transmitted signal is a 10GHz sinusoidal signal of the form,

$$T_x(t) = A * \cos(2 * \pi * 10 * 10^9 * t + \varphi) \tag{3.1}$$

Where Φ is the phase of the transmitted signal and A is the signals amplitude calculated in Eq. 3.2.

$$A = Vrms = \frac{Vpp}{2 * \sqrt{2}} \tag{3.2}$$

Scalar spectrum analyzers often present the amplitude in terms of signal power referenced to 1mW or Decibels-milliwatts (dBm):

$$dBm = 10 * log_{10}\left(\frac{Vrms^2}{R * p_0}\right) \tag{3.3}$$

where R = signal input impedance = 50 Ω and Po = 1 mW.

The amplitude measurement displayed by a scalar spectrum analyzer contains no phase information about the sinusoidal input signal. Therefore, using the HP8559A, only the amplitude, power and frequency of the NFMWI Rx signal can be extrapolated.

3.1.1. HP8559A Phase Measurement Simulation

Consider the following feasibility test. A Tektronix AFG3102 arbitrary function generator was used to simulate the Rx signal of the NFMWI system. The function generator was configured to supply a 7 100MHz, 1 Vpp, 0 phase shift sinusoidal signal. The signal was supplied to an Agilent 8463E scalar spectrum analyzer. Using Eq. 3.4 the amplitude of the signal is,

$$A = \frac{1}{2 * \sqrt{2}} = 0.353\ Vrms = 10 * log_{10}\left(\frac{0.353^2}{50 * 0.001}\right) \approx 3.98dBm \qquad (3.4)$$

Figure 3.1 shows the screenshots of the function generator signal and the frequency vs. amplitude curve measured by the Agilent 8463E.

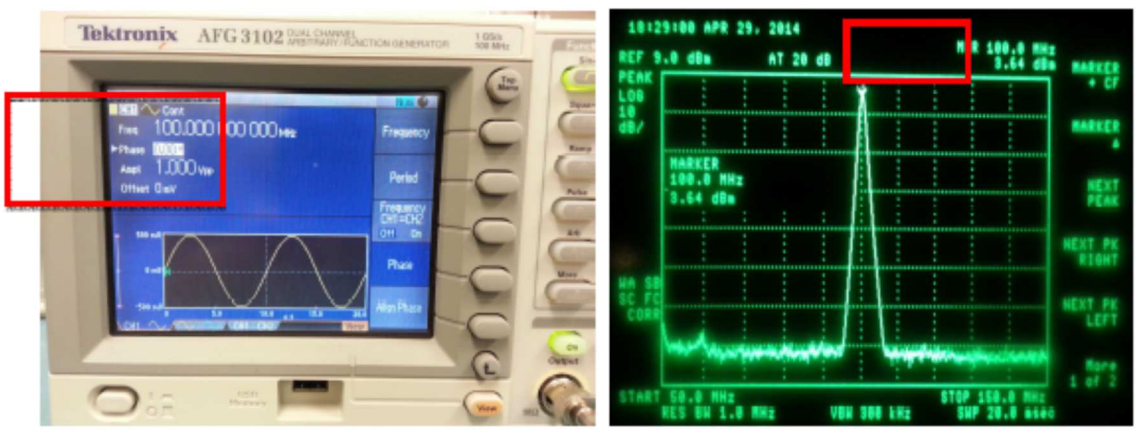

Figure 3.1 NFMWI Phase Measurement Simulation: Rx Signal (right); Scalar Spectrum Analyzer Measurement (left)

The red boxes on Figure 3.1 highlight the properties and measurements of the simulated Rx signal on their respective devices. The Agilent 8463E measured an input signal with an amplitude of 3.64 dBm and a frequency of 100MHz. The spectrum analyzer reports no information on the phase of the input signal.

Ideally, the test sample scanned by the NFMWI will impose a phase difference between the Tx and Rx signals. In order to simulate this, a phase shift of 90 degrees was attributed to the signal produced by the function generator. Figure 3.2 shows the screenshots of the function generator signal with added 90 degrees phase shift and the amplitude vs. frequency curve measured by the Agilent 8463E.

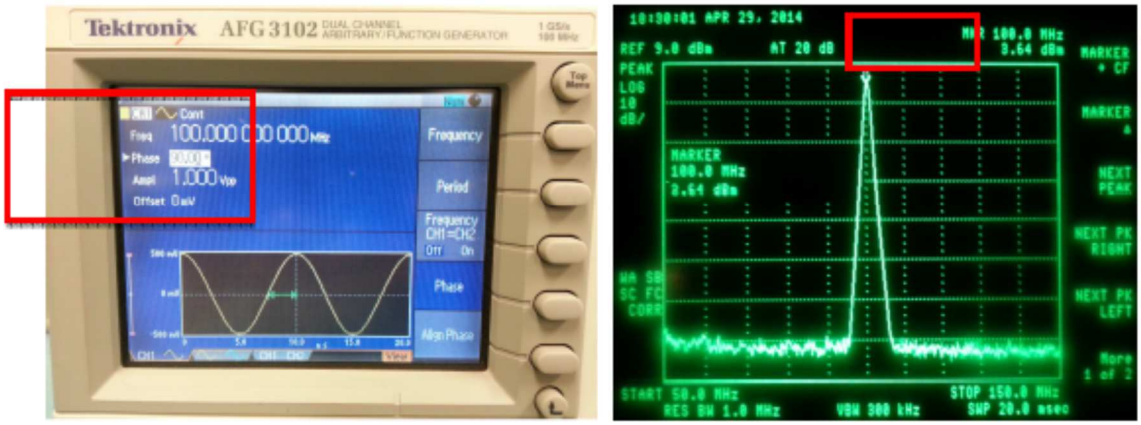

Figure 3.2 NFMWI Phase Measurement Simulation: 90 degrees Phase Shift Rx Signal (left); Scalar Spectrum Analyzer Measurement (right)

The red boxes on Figure 3.2 highlight the properties and measurements of the simulated Rx signal on their respective devices. Though a 90 degrees phase difference was added to the input signal, the spectrum analyzer makes the exact same measurements seen in Figure 3.2.

There's a discrepancy between the calculated power of the Rx signal and what was measured by the Agilent 8463E. This measurement is potentially caused by variances in the impedance of the output port of the signal generator and or the input port of the spectrum analyzer. Both ports are listed at 50Ω.Also, power discrepancy could be related to user error. Nevertheless, the function generator was configured to display the power of its output signal seen in Figure 3.3.

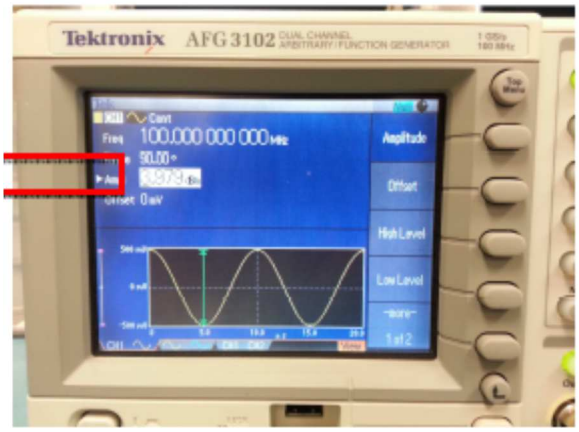

Figure 3.3 Output Signal Power Displayed on the Function Generator

The Agilent 8463E interprets the simulated Rx signal with and without phase difference exactly the same. The scalar spectrum analyzer does not preserve the phase or temporal information of an input signal. Since the HP8559A is a scalar spectrum analyzer it is strongly inferred that it won't capture this information either. Alternate approaches are required in order to measure the phase information of a test sample scanned by the NFMWI system.

3.2. Phase Information Acquisition Approaches

3.2.1. Background

In order to measure the phase difference between two signals, both signals need to have the frequency and shape.

3.2.2. Pre-Requisite Information

Use the spectrum analyzer to get an idea of the power level of the received signal. Transmitted signal power can be controlled by output dBm level on signal generator. Once received power levels are known. Transmitted and received signals should be measured with an oscilloscope. Software and a communication bus will be used to query the trace of each signal. The software will perform post processing to determine the spectrum of each signal. These spectrums will be compared to the spectrums measured by the spectrum analyzer to ensure confidence in software.

3.2.3. Analog Mixing

Frequency mixing is an Analog phase detection technique that is used to measure phase difference between two signals with same frequency. For our purpose these two signals are the transmitted signal (Tx) and the reflected signal (Rx). This approach is simply achieved by feeding these two amplitude limited signals into a product detector and the output of the detector will represent the phase difference between the signals after filtering out high frequencies.

3.2.4. Mathematical Model

$$T_x(t) = A_1 * \cos(2 * \pi * 10x10^9 * t) \tag{3.5}$$

$$R_x(t) = A_2 * \cos(2 * \pi * 10x10^9 * t + \Phi) \tag{3.6}$$

The product of Tx and Rx is,

$$V_p(t) = T_x(t) * R_x(t) = \frac{k\,A_1 A_2}{2}\,[cos\,(2 * \pi * 20x10^9 * t) + cos(\Phi)] \tag{3.7}$$

Notice that the output contains a double frequency component and a DC component that is only a function of the phase difference between the two signals. The high frequency will be filtered out using low pass filter and the remaining DC is as follow.

$$V_p(t)(\text{Filtered}) = \frac{k\,A_1 A_2}{2}\,[cos(\Phi)] \tag{3.8}$$

3.2.5. Analytical Analog Mixing Approach

A monopole probe in transceiver mode is being used to transmit and pick up the reflected signals from the sample. The application of the two, .i.e. the incident and the reflected wave signals to a mixer (multiplier) inputs results in a dc signal at the output port. This output contains a sum and difference of the frequencies applied at the inputs. Their sum can be filtered out using a low-pass filter. The difference is zero Hz, or dc, which is proportional to the difference in phase between the input signals.

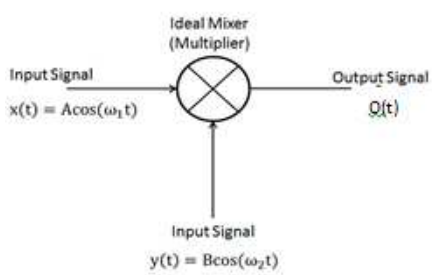

Figure: Mixer/ Multiplier

$$O(t) = Acos(\omega_1 t + \theta).B\cos\,(\omega_2 t)$$

$$O(t) = \frac{AB}{2}[cos(\omega_1 t + \omega_2 t + \theta) + cos(\omega_1 t - \omega_2 t + \theta)]$$

$$\omega_1 = \omega_2$$

$$O(t) = \frac{AB}{2}[\underbrace{cos(2\omega t + \theta)}_{\text{Signal oscillates @ 2*f which should be filtered}} + \underbrace{cos(\theta)}_{\text{DC Offset}}]$$

Figure 3.4 Illustration of phase detection methodology through complex demodulation approach.

In Figure 3.4, O(t) contains energy at sum and difference frequency. Mixing is non-linear operation, so O(t) has harmonics of the input signals. The real-world O(t) contains a

fundamental freq. and a number of sum and different harmonics, and θ is the phase different between input signals

3.2.6. Numerical MATLAB Mixer Method

We simulated ideal mixers and assumed that no electrical losses were factored into simulation. We defined two analog signals T_x as the transmmited and R_x as the Received signals, both are at 10GHz. T_x and R_x were multiplied together and the product results the following:

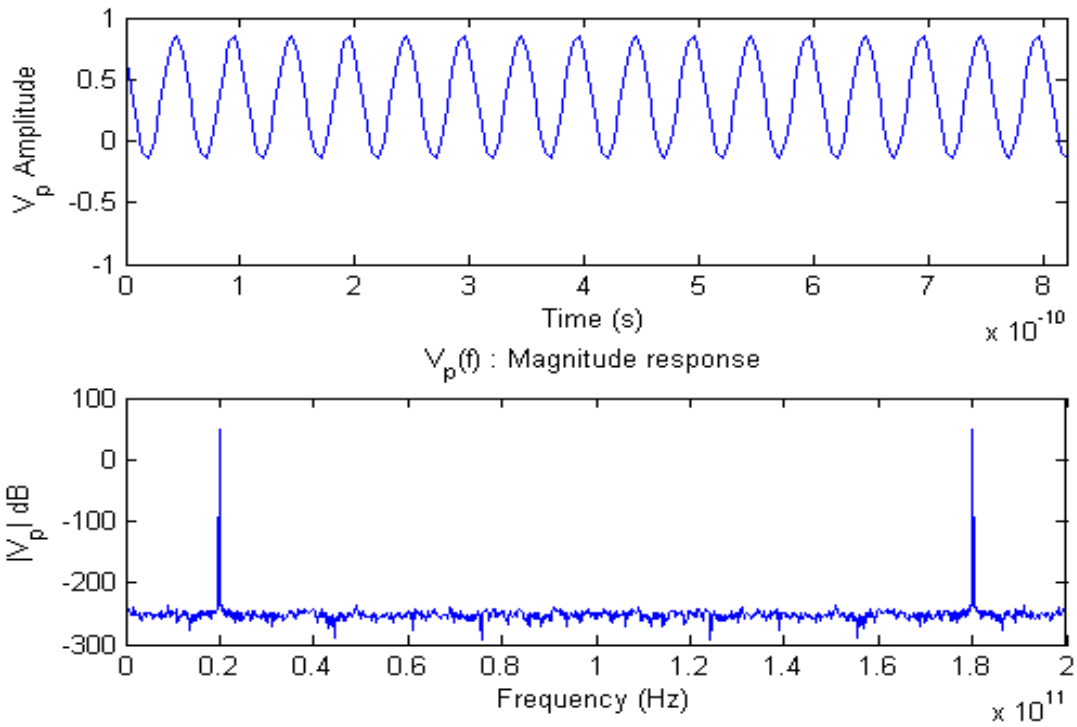

Figure 3.5 The output is double frequency at 20 GHz floating around a DC value.

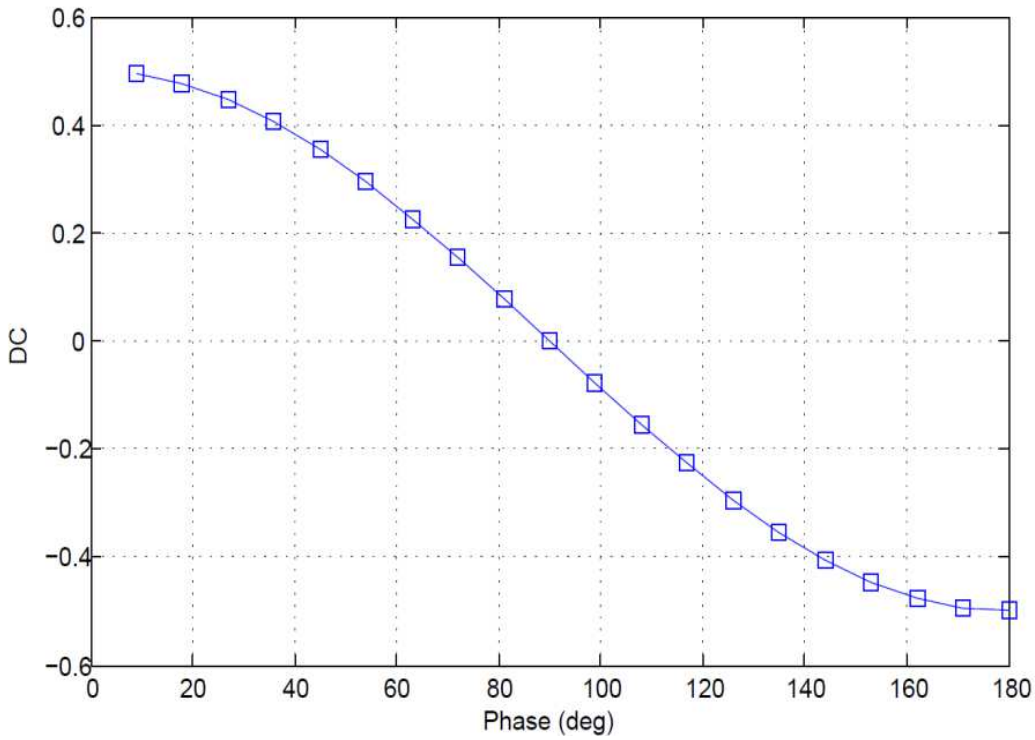

Figure 3.6 Phase diff. between signals varied 0 to 180 deg. in 9 deg. intervals.

3.2.7. LTSPICE Double Balanced Diode Ring Mixer

A more accurate model of mixer's actual performance. The schematic of the simulated circuitry and output signals are shown in Figure 3.7(a) and Figure 3.7(b).

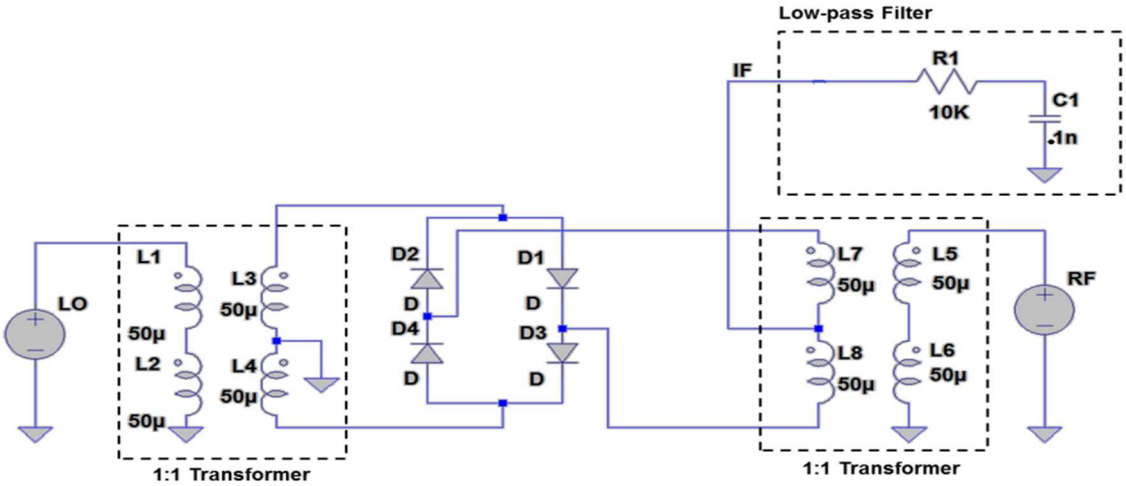

(a)

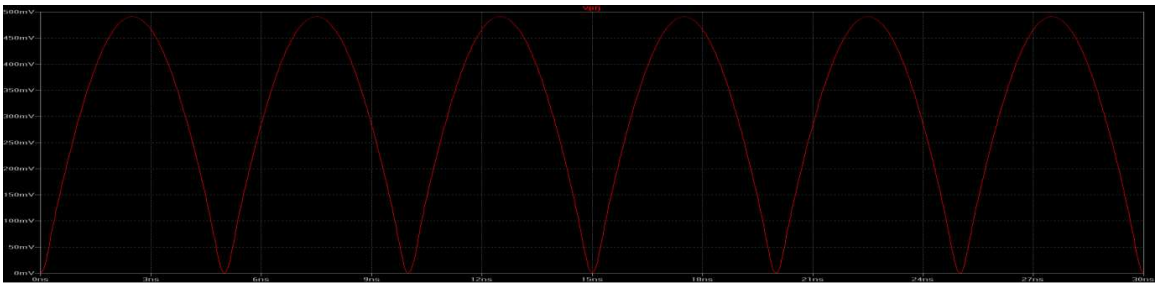

(b)

Figure 3.7 (a) Double Balanced Diode Ring Mixer Schematic and (b) the output is double frequency at 20 GHz.

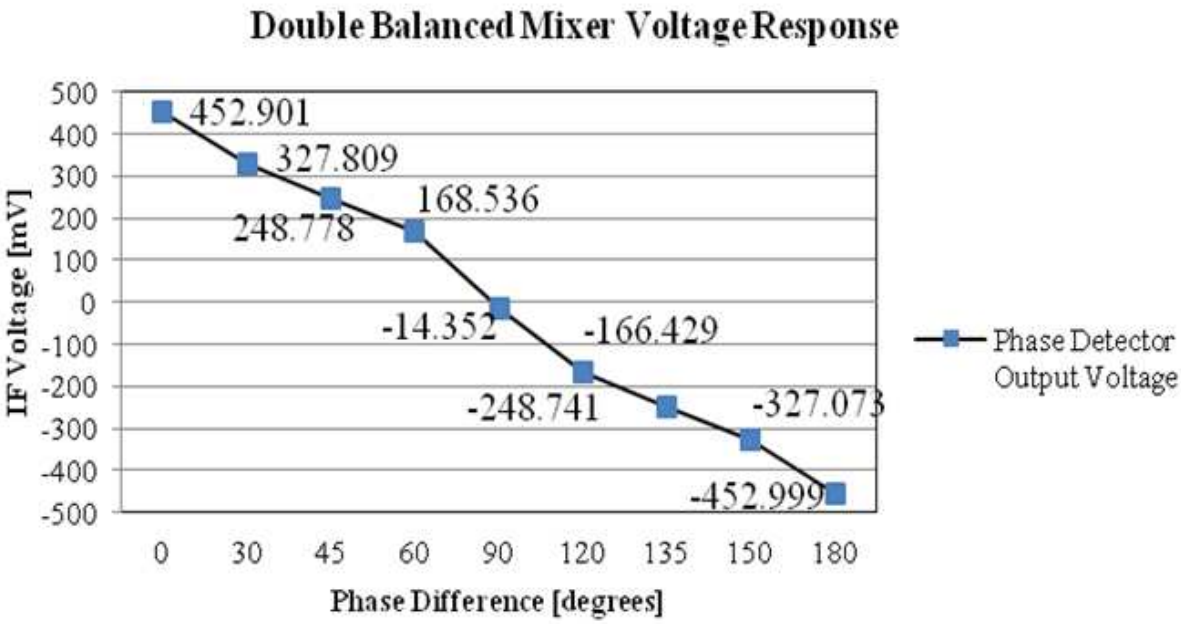

Figure 3.8 IF voltage measured at each phase diff. increment from 0 deg. To 180 deg.

3.2.8. Phase Detection using SM1717 Mixer

After successfully simulation validation and studies, hardware implementation was conducted using Siga Tek SM1717, which is a microwave double balanced mixer offers high isolation and low loss. It takes two inputs i.e. RF and LO and gives its output on IF. The mixer electrical specifications are shown in Table 1 as follows:

Signal	Type	I/O	Description
Radio Frequency (RF)	AC	Input	LEAP NFMWIS Rx signal
Local Oscillator (LO)	AC	Input	LEAP NFMWIS Tx signal, drives mixer electronics
Intermediate Frequency (IF)	AC	Output	

Electrical:	Specifications:
RF:	4.0 - 12.4 GHz
LO:	4.0 - 12.4 GHz
IF:	DC - 2.0 GHz
LO Drive:	17 dBm Typ
Conversion Loss:	7.0 dB Typ
Isolation L-R:	25 dB Min
Isolation L-I:	20 dB Min

Table 3.1 Specifications for the SM1717 Mixer.

One experiment was conducted to study mixer behaviors and its output responses with input phase difference, in which the mixer was connected according to the following diagram in Figure 3.9. As demonstrated in Figure 3.9, there is an insignificant error in measurements due to harmonic distortions but the overall phase detection performance is satisfactory.

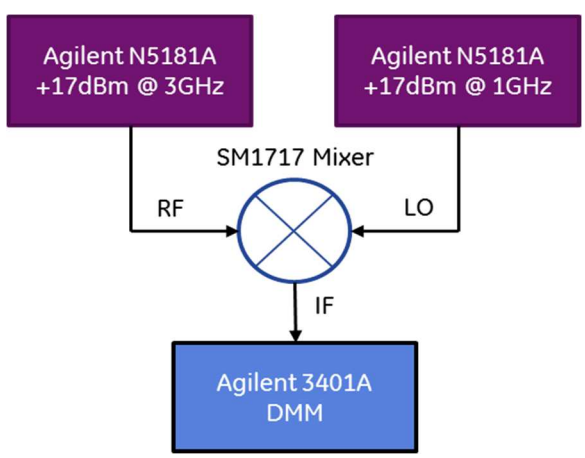

Figure 3.9 Experimental IF voltage measurement schematic.

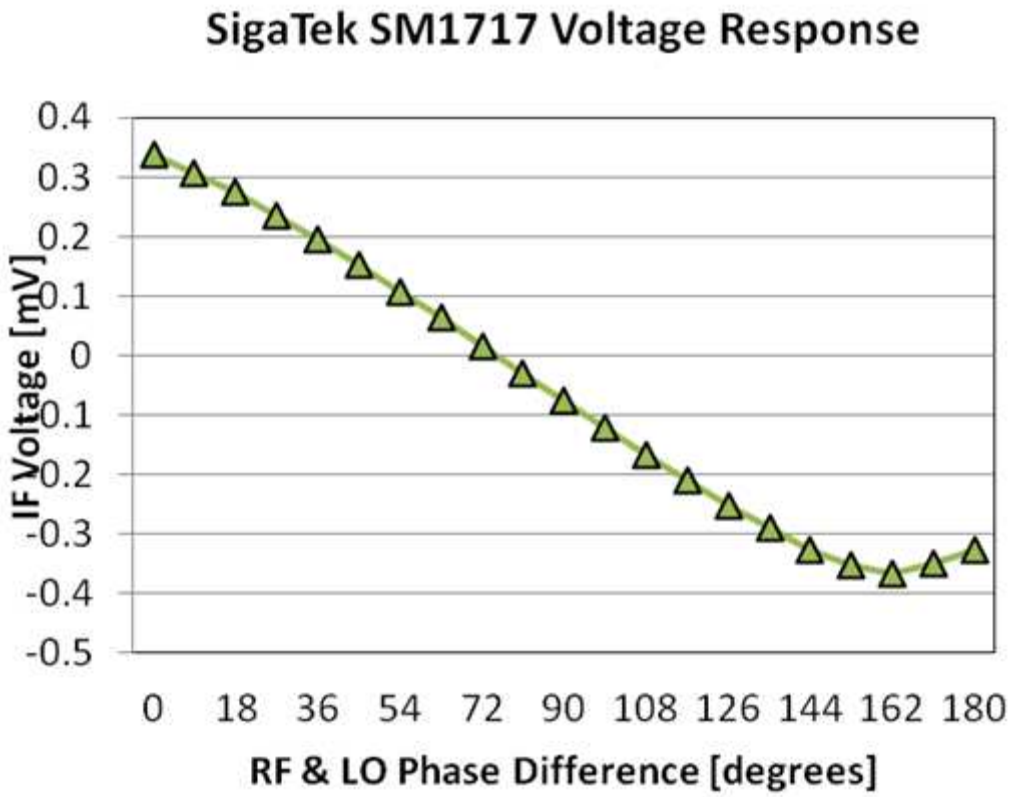

Figure 3.10 IF voltage measured at each phase diff. increment from 0 deg. to 180 deg.

3.3. Phase Detection System Prototyping for Piping Materials Characterization

The following part presents the practical implementation of the phase detection approach. A block diagram of the system with signal flow and laboratory setup is presented in the following Figure 3.11.

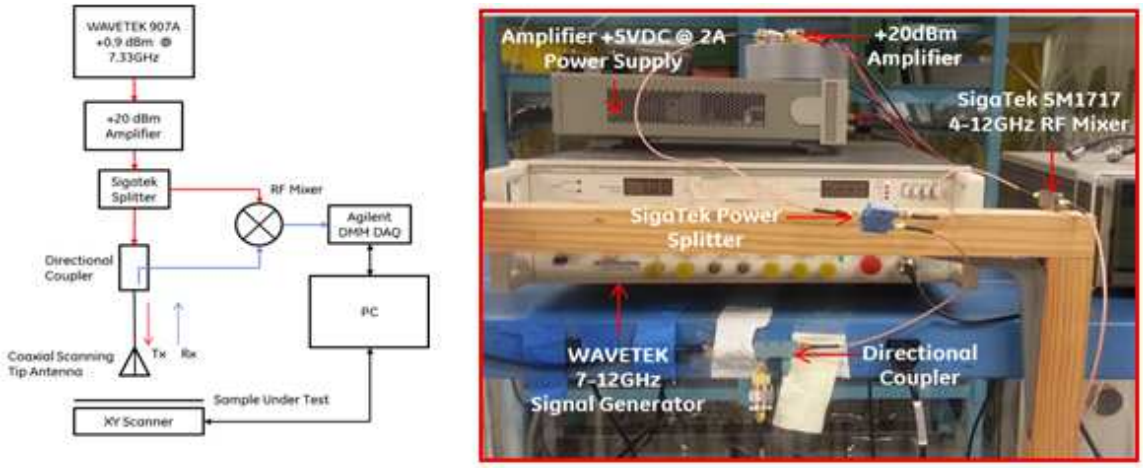

Figure 3.11 LEAP NFMWI Phase Detection block diagram and hardware setup

The following results were obtained with the following setups:

1. Mid-size Triangle of Al calibration sample was imaged, illustrated in Figure 3.12
2. Waveguide lift-off distance ≈ 3mm from DUT, Tx = 10GHz
3. 2D scan was performed using raster-scan mode and phase maps of the DUT were successfully generated.

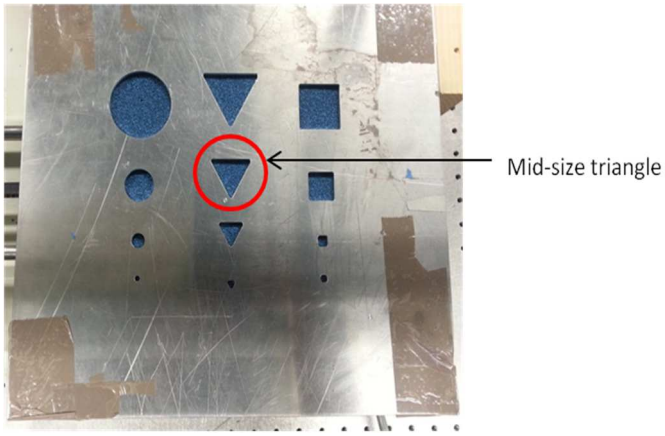

Figure 3.12 Mid-size Triangle of Al calibration sample

The initial LEAP NFMWI phase approach results are shown in Figure 3.13.

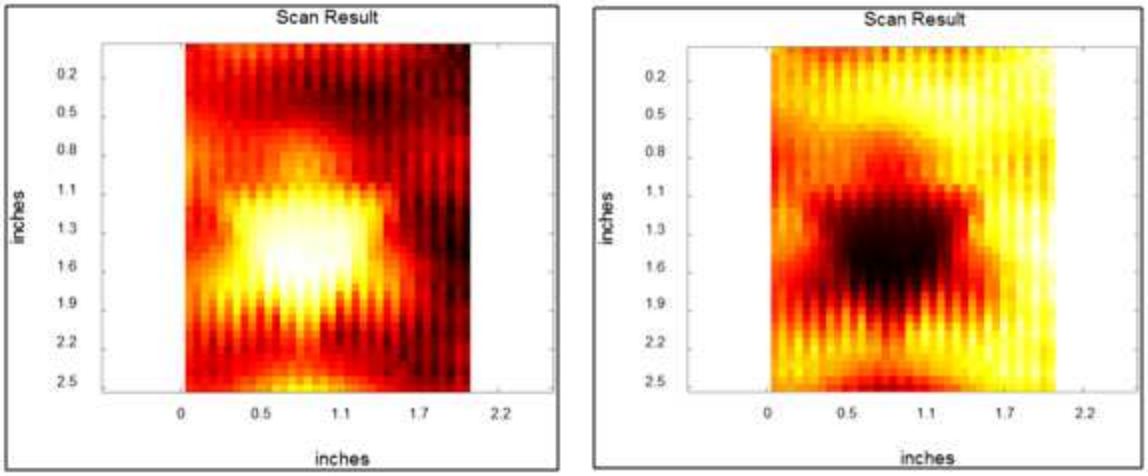

(a) (b)

Figure 3.13 (a) Image of Mixer IF voltage measurements and (b) corresponding image of Phase Differences after post-processing.

These results are promising and the team were encouraged to proceed forward and scan the whole calibration sample with longer scanning time. The scan with same setup produced the following results in Figure 3.14.

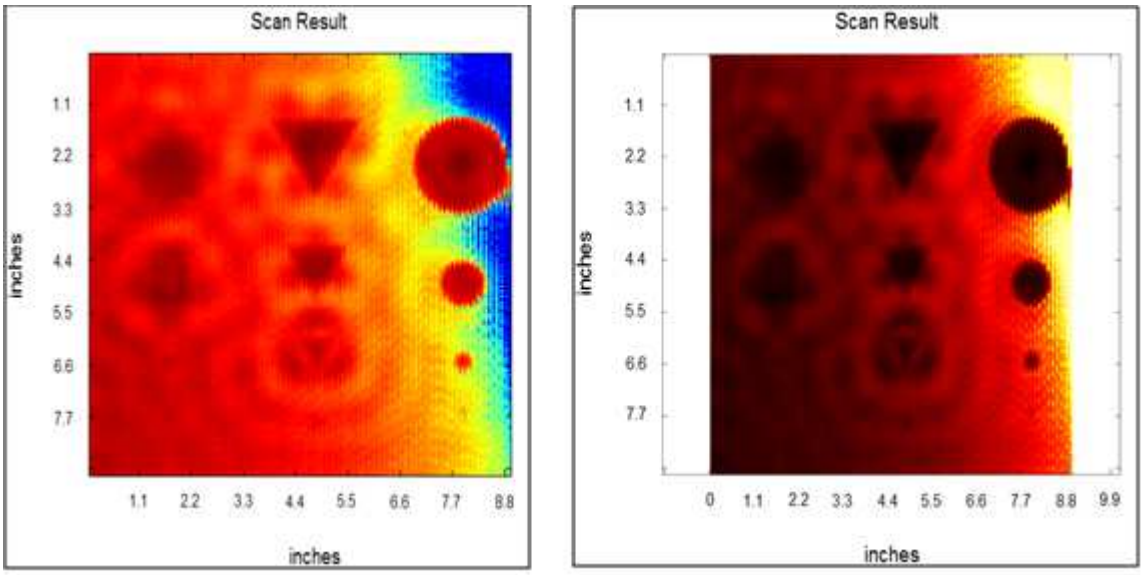

(a) (b)

Figure 3.14 Resulting image of the entire calibration sample: (a) image of Mixer IF voltage measurements and (b) corresponding image of Phase Differences after post-processing.

As the results show resolving circles and triangles was acceptable but squares are hard to make out. After the initial images were obtained, the research continued forward to optimize the acquisition parameters for better image quality. By optimizing the liftoff distance between the probe and the sample the following results shown in Figure 3.15 were acquired.

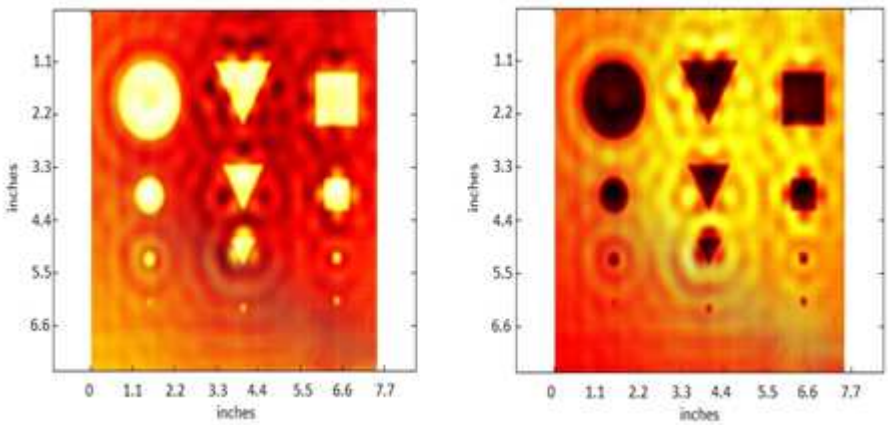

(a) (b)

Figure 3.15 Resulting image of the entire calibration sample after parameters optimization: (a) image of Mixer IF voltage measurements and (b) corresponding image of Phase Differences after post-processing.

It is concluded that phase information revealed a high resolution special images and it is capable to provide information that is not possible from only amplitude data. Phase information extraction using frequency mixing is inexpensive, easy to implement approach. By using RF Siga Tek SM1717, LEAP was capable to extract phase information of the scanned sample to construct 2D images that represent variation in the sample properties. High resolution Images were abstained and presented in this report.

Currently, LEAP team is pursing to improve scan efficiency. The team is working to utilize fast imaging capability using sparse signal reconstruction, e.g. compressed sensing based approach to improve scan timing without compromising the image resolution. We use frequency mixing approach to measure the difference in phase between the incident and reflected signals. This is a very affordable and simple method to extract fruitful information from the scanning results, including the properties of DUT, and if any abnormalities present. Figure 3.16 shows phase map result of a coin hidden under HDPE.

From Figure 3.16(c) we can see a circular shape at where the coin located under the HDPE sample. This also matches the result we got before from amplitude scan, which approves the capability of microwave for penetrating through the sample (at 1.56cm).

(a) (b) (c)

Figure 3.16 Phase map result of a coin hidden under HDPE. (a) HDPE sample (b) HDPE sample with coin (c) Scanning results

We also did several other scans using optimized phase scan measurements. Figure 3.17 shows the phase scan result of a Carbon Fiber Reinforced Polymer(CFRP). The result shows that we are able to reveal the CFRP pattern on top of the sample. Due to the high conductivity of the sample, we still need to do more experiments to verify the skin depth for this material.

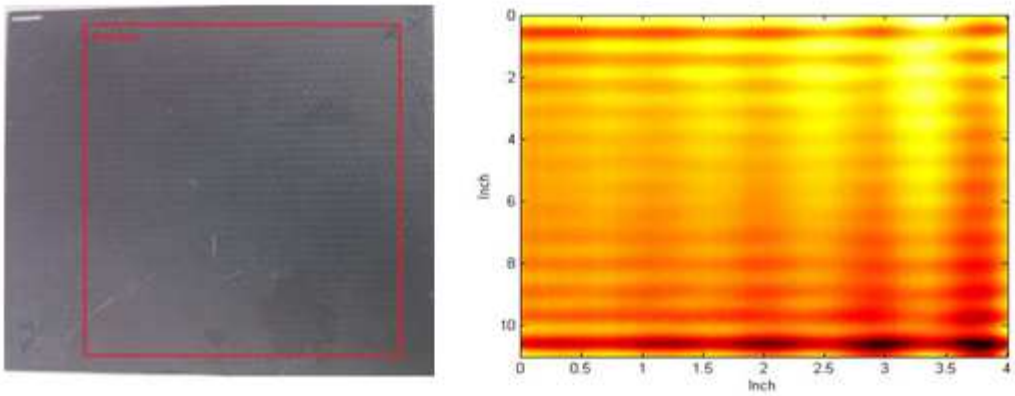

(a) (b)

Figure 3.17 Phase scan result for CFRP.(a) Carbon Fiber Reinforced Polymer sample. (b) Phase scan result

LEAP has utilized a 3D printing technology to print 3D plastic sample. Defects were introduced as air gaps with different sizes and at various depths of the sample, as shown in Figure 3.18(a). The phase scan information result shows in Figure 3.18(b). From the results, we can only clearly see two square subsurface defects, which are in the middle of the sample, the other visible defect is on the bottom right of the sample.

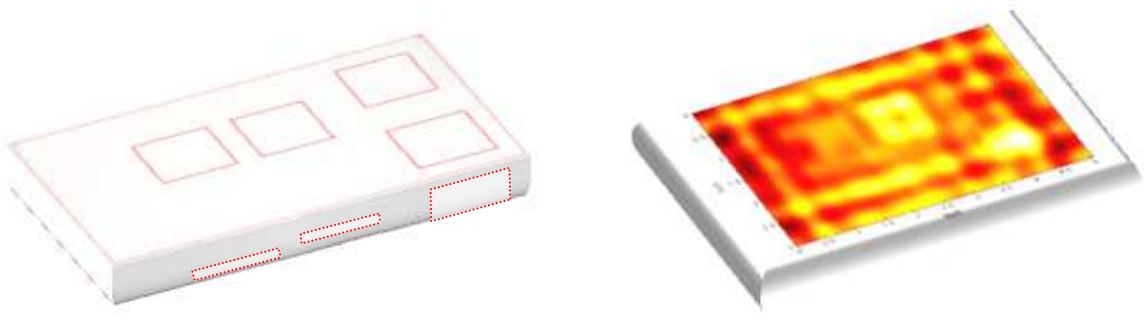

(a) (b)

Figure 3.18 Phase scan result for 3D plastic printing sample.(a) 3D plastic printing sample. (b) Phase scan result

Meanwhile, a calibration sample with 6 holes was scanned. Each hole on the sample has a diameter of 1cm. The fourth hole also has a small slot with size of 0.75mm by 3mm as defect, shown in Figure 3.19(a). The scanning result can clear see the holes on the sample, and also shows the small defect on the fourth hole, which again demonstrates that the LEAP microwave imaging system has the ability to detect sub mm defects .

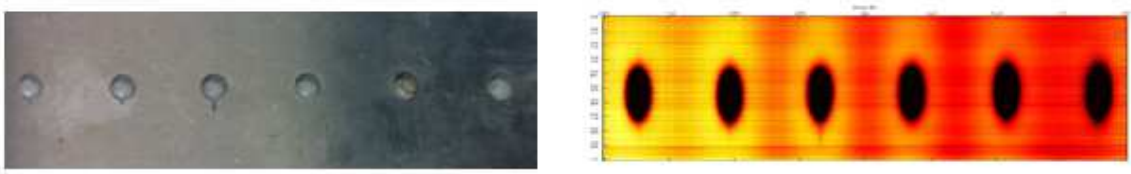

(a) (b)

Figure 3.19 . Scan result of calibration sample with 6 holes.(a) Calibration sample with 6 holes. (b) Phase scan result

.

CHAPTER 4 PARAMETRIC STUDY FOR NEAR FIELD MICROWAVE IMAGING SIMULATION

4.1. FEKO Simulation for Single Channel Sensor

Simulation study is an important way to assist experimental studies and sensor development via optimization of critical parameters. In this 4th quarter, we are continuing in developing a dedicated model to simulate the experiment setup for plastic piping material loss imaging using NFWMI by measuring the total electromagnetic fields between the sensors and the sample under test (SUT). Figure 4.1(a) and Figure 4.1(b) show the simulation model geometry for defective (simple through circular hole geometry) and homogeneous SUT, respectively.

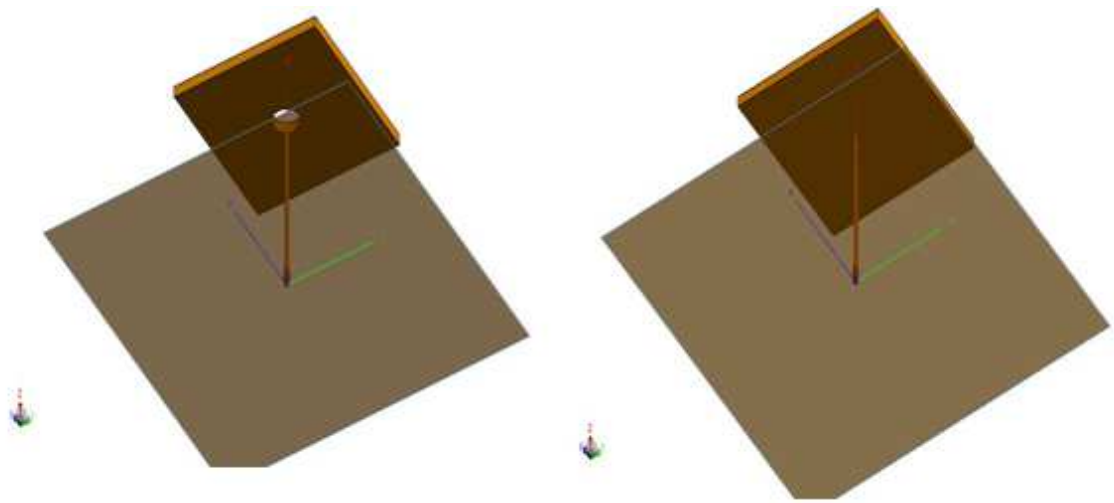

(a) (b)

Figure 4.1 Simulation model with different SUT geometry: (a) PEC material with a through circle at the center. (b) homogeneous PEC material

Due to the limitation of the software our group obtained in the past Quarter, some parameters, i.e., the number of discreted points used in the model is smaller than the actually measurement data points in the experiment setup. In the simulation model, a monopole antenna is used to simulate the probe tip, whose diameter is 0.2mm. The cutoff frequency of the antenna is set at 10GHz, so the size of the monopole antenna is calculated as a quarter of the radiation wavelength, which is 7.5mm. The size of the PEC board is 8mm x 8mm x 0.5mm. The monopole antenna is placed at the central line of the SUT and moves along in the x direction

while numerically predicting electric field values. The radiation pattern of the monopole antenna shows that the radiation power is concentrated at the tip of the near field microwave antenna as desired. Then, we calculated the power between the probe tip and SUT. Since the only difference between two modeling geometry is the through hole defect at the center of the SUT, the defective SUT with a through hole should generate higher electric field intensity around antenna tip due to antenna radiates more power penetrating through the target. Figure 4.2 shows the simulation result that was generated from the developed models in Figure 4.1(a). It validated that at the center of the SUT, the measurement signal can capture the defective signature and it also proves that the simulations match our proposed theory and research hypothesis for this CAAP project.

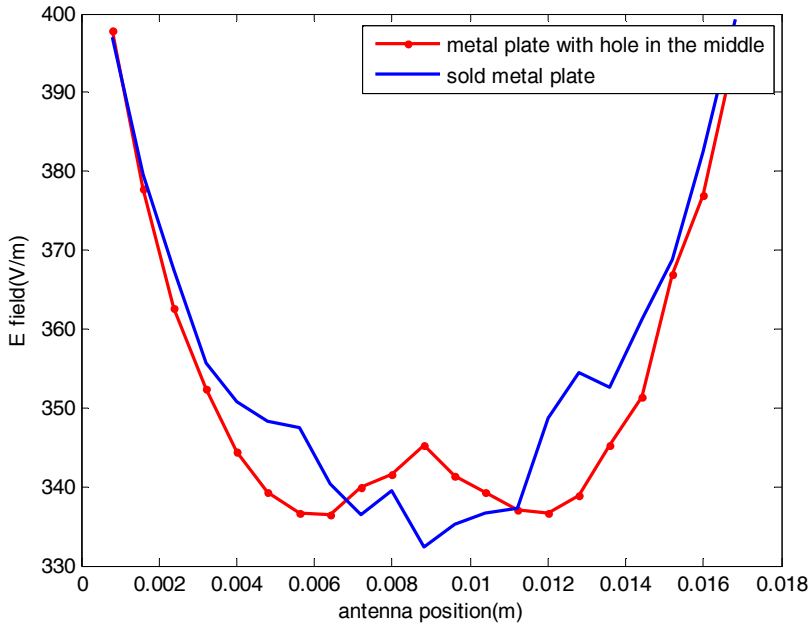

Figure 4.2 Simulated electric field intensities along x direction of scanning

4.2. FEKO Simulation for Multi - Channel Sensor

The goal of the project is to develop a model of multi-channel NFMW sensors to improve the scanning speed and field of view (FOV) by collecting data in multiple directions at the same time. The goal of the simulation is to study the radiation pattern of each channel by optimizing the operating parameters. The multi channel NFMW sensor is

designed by using several monopole antennas mounted on a pipe shaped (cylindrical) tube so the inside of the pipe can be effective imaged.

Before we design the circular shape multi channel scanner, we tried to make a scanner on a flat surface to verify if there are any affect made by the circular shape tube. Figure 4.3 shows the geometry of the flat surface scanner. Length of antenna is still 2.5cm, size of the flat surface is 3 wavelengths x 12 wavelengths, the space between each antenna is 1.5 wavelength. Figure 4.4 shows the near field of each antenna. The result shows each antenna has the ability to reach the same level of radiation. The two on the side has higher E field than others because of the edge effect, which is able to reduce by changing the size of ground plate and also try other type of boundary conditions.

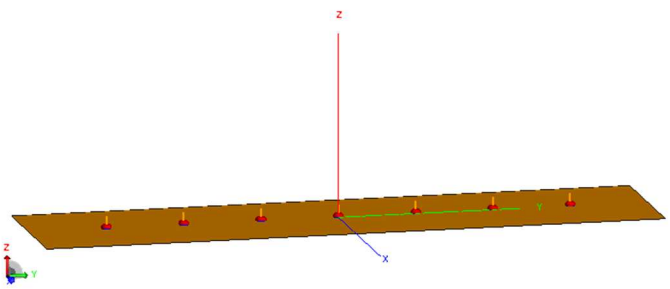

Figure 4.3 Geometry of a flat surface multi channel scanner

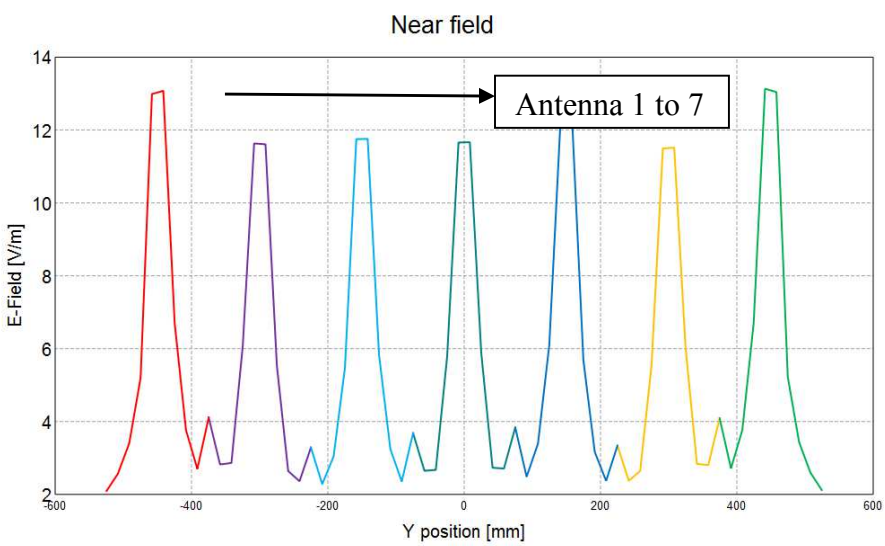

Figure 4.4 Near field of each antenna of flat surface multi channel scanner

Then we built the 12 channel NFMW scanning sensor on a circular tube. Figure 4.5(a) shows the geometry of the sensor. The diameter of the circular scanner is 25.4cm, the scanner is operating at 3GHz. The diameter of the circular scanner will design according to different size of pipe diameter. Figure 4.5(b) shows the radiation pattern of each antenna. Even though the scanner was putting in a homogenous environment, the field pattern is not really symmetric in the system. There are a couple reasons. First, the surface of circular shape scanner is not actually perpendicular to the antenna, which will cause reflections from the PEC surface. Second, the size of mesh is not fine enough to match the field to where the antenna located at, which is limited by the current computing power.

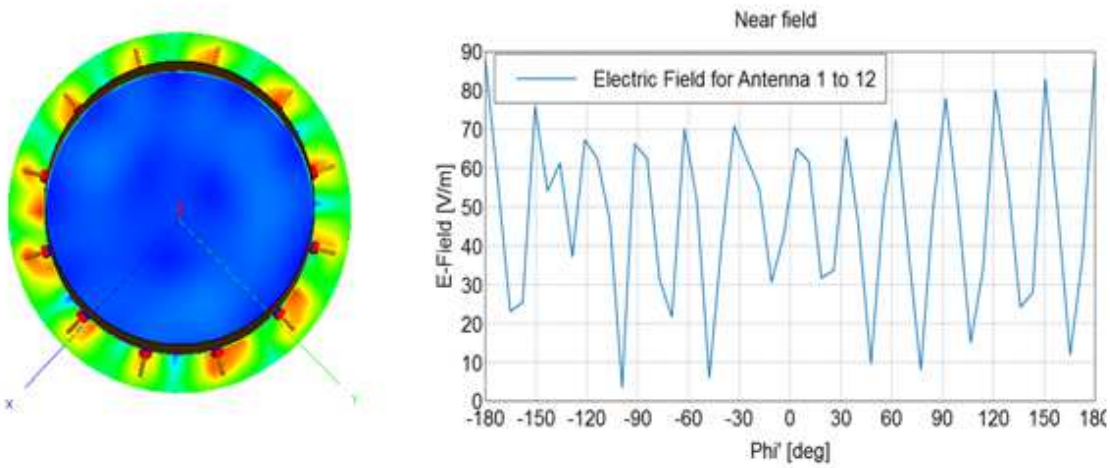

(a) (b)

Figure 4.5 Simulation model for 12 channel NFMW sensor.(a) Geometry of design. (b) Near field

4.3. HFSS Simulation for Single Channel Sensor

To validate the simulation results, we developed another model with same geometries in HFSS, to simulate the sensors performance and facilitate the proposed sensors prototyping task. HFSS is the software for simulating 3D full-wave electromagnetic fields, which is essential for designing high-frequency and/or high-speed components used in modern electronics devices. It uses finite element method (FEM) to calculate the fields around antenna; the automatic adaptive meshing technique provides a mesh that is conformal to the 3-D structure and appropriate for the electromagnetic problems. So to verify the results, we

repeated the simulation we did using FEKO. First we repeated the simulation for a simple monopole antenna at 3GHz. The monopole antenna is mounted onto a SMA connector, which is similar to our experiment design. Figure 4.6 shows the geometry of a single monopole antenna, reflection coefficient, and field radiation of monopole antenna.

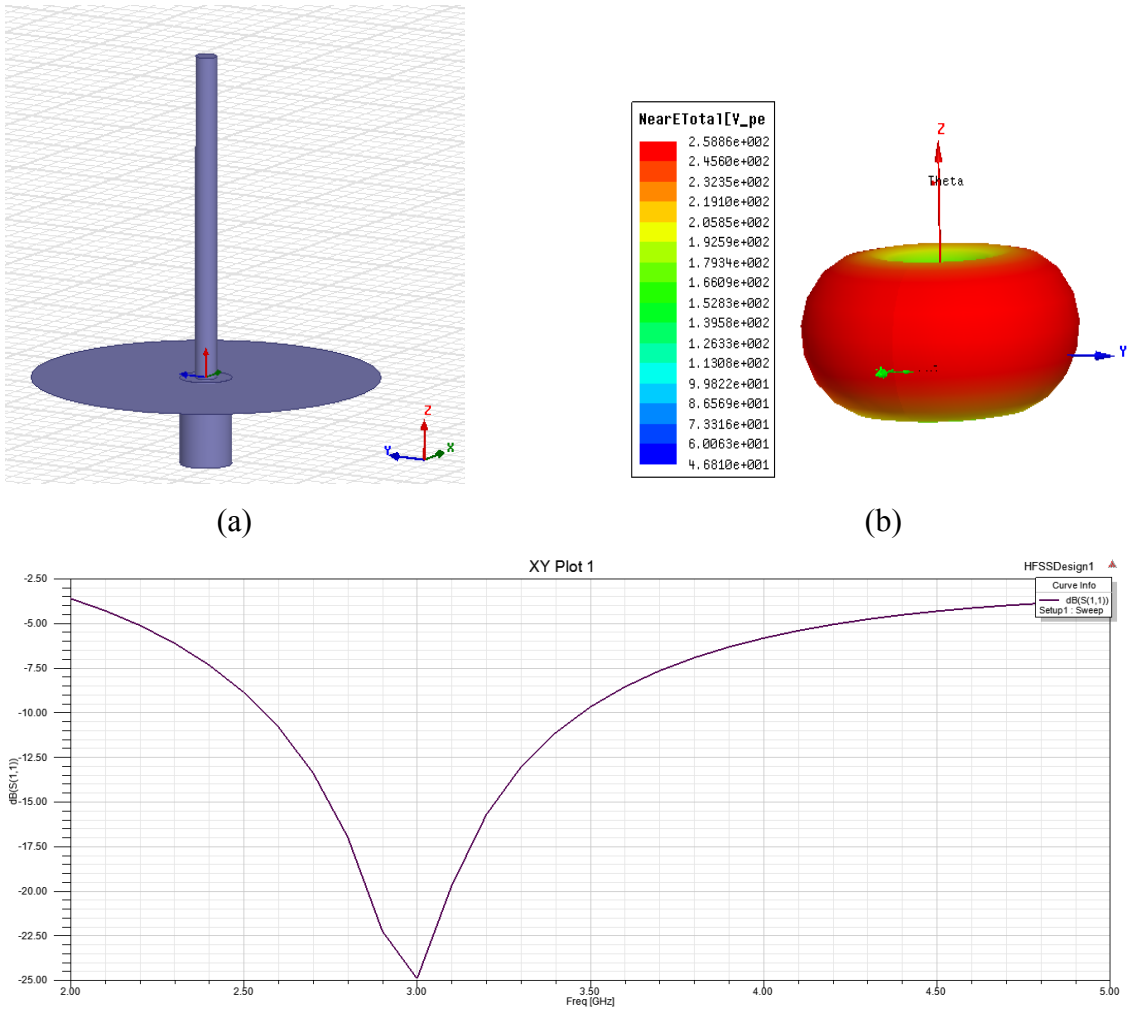

Figure 4.6 Simulation model for single monopole antenna.(a) Geometry of design. (b) Near field radiation pattern. (c) Reflection coefficient of antenna

The obtained field pattern and reflection coefficient shows that the monopole antenna is transmitting signal at 3GHz as desired.

Next step is to simulate the multi-channel sensor for understanding and optimizing the system design. First we simulate the pipeline imager with a flat surface for feasibility study only. There are 7 antennas mounted on the surface of the metal (grounding plate) which

are 1.5 wavelengths apart from each other, this is exactly the same as model geometry in FEKO simulations. Figure 4.7(a) shows the geometry of the flat surface NFMM scanner. From Figure 4.7(c) we can tell that each antenna has the same reflection coefficient, and they all resonate at 3GHz. Figure 4.7(b) shows the simulation results for near field interrogation, in which the field strength increases from the bottom of the antenna to the tip. The field pattern demonstrated that the high power is concentrated at the tip of sensor array, and they are equally radiated. This results matched the one we had from FEKO, and gave us the confidence to move forward in sensing elements fabrication, and the next prototype geometry will be a multi-channel sensor array with cubic shape.

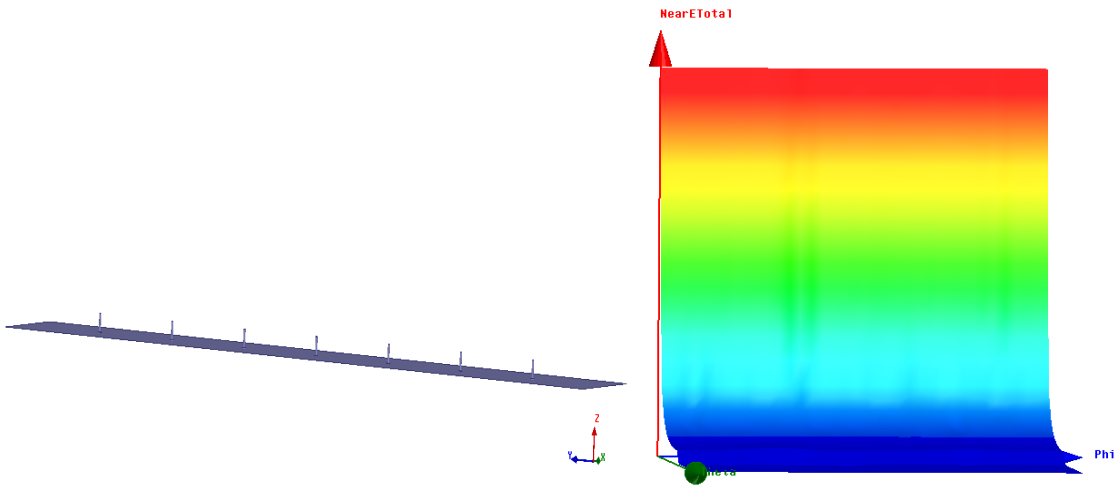

(a) (b)

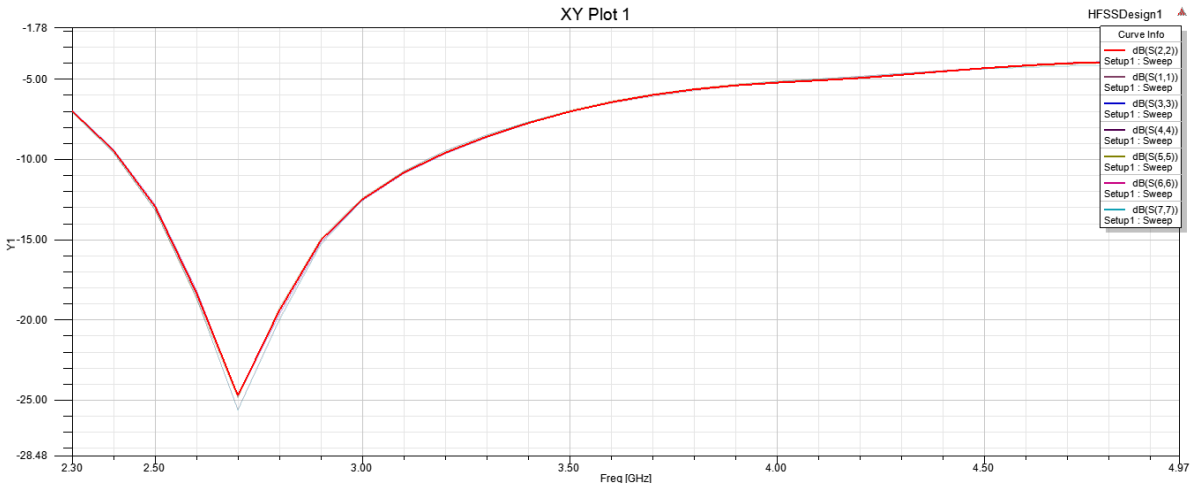

(c)

Figure 4.7 Near field of flat surface multi channel scanner (a) Geometry of the sensor array on a flat surface. (b) Near field magnitude result of the sensor array. (c) Reflection coefficient of each antennas

Figure 4.8 (a). shows the geometry of a cubic shaped multi-channel CTA sensor array. The length of each side is 4cm. The 4 sides of the cubic used as ground plane with SMA connectors. The antennas are located at the center of each sides. The antennas are still designed to resonate at 3GHz.

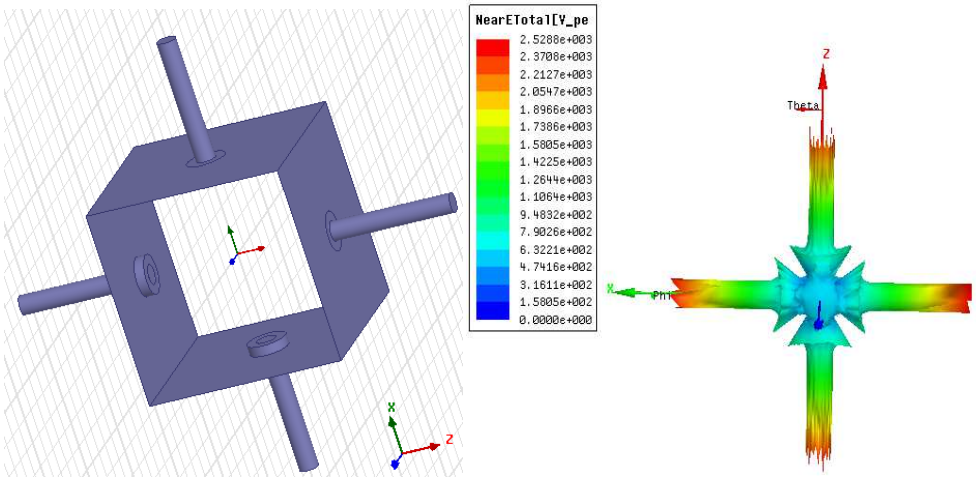
NearETotal[V_pe
2.5288e+003
2.3708e+003
2.2127e+003
2.0547e+003
1.8966e+003
1.7386e+003
1.5805e+003
1.4225e+003
1.2644e+003
1.1064e+003
9.4832e+002
7.9026e+002
6.3221e+002
4.7416e+002
3.1611e+002
1.5805e+002
0.0000e+000
Z
Theta
Phi
X
Y

(a) (b)

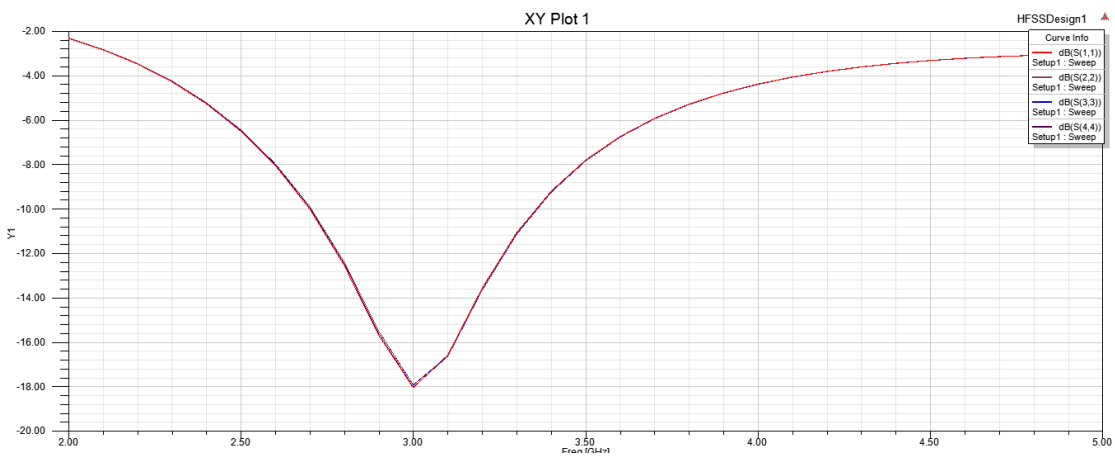
XY Plot 1
HFSSDesign1
Curve Info
dB(S(1,1))
Setup1 : Sweep
dB(S(2,2))
Setup1 : Sweep
dB(S(3,3))
Setup1 : Sweep
dB(S(4,4))
Setup1 : Sweep
Y1
-2.00
-4.00
-6.00
-8.00
-10.00
-12.00
-14.00
-16.00
-18.00
-20.00
2.00
2.50
3.00
3.50
4.00
4.50
5.00

(c)

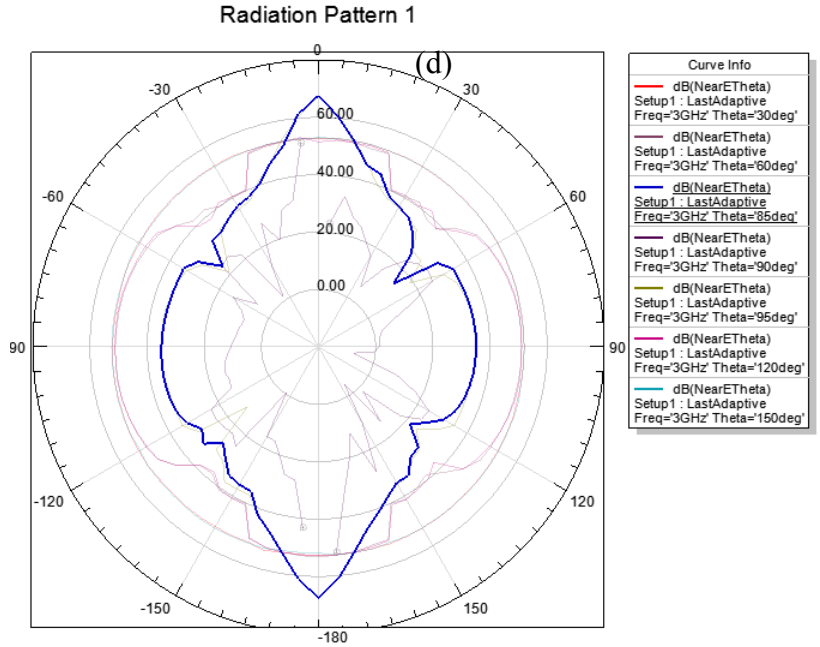
Radiation Pattern 1
0
30
60
90
120
150
-180
-150
-120
-90
-60
-30
60.00
40.00
20.00
0.00
Curve Info
dB(NearETheta)
Setup1 : LastAdaptive
Freq='3GHz' Theta='30deg'
dB(NearETheta)
Setup1 : LastAdaptive
Freq='3GHz' Theta='60deg'
dB(NearETheta)
Setup1 : LastAdaptive
Freq='3GHz' Theta='85deg'
dB(NearETheta)
Setup1 : LastAdaptive
Freq='3GHz' Theta='90deg'
dB(NearETheta)
Setup1 : LastAdaptive
Freq='3GHz' Theta='95deg'
dB(NearETheta)
Setup1 : LastAdaptive
Freq='3GHz' Theta='120deg'
dB(NearETheta)
Setup1 : LastAdaptive
Freq='3GHz' Theta='150deg'

(d)

Figure 4.8 Near field of cubic shape multi-channel NFMM scanner (a) Geometry of the cubic shape sensor array. (b) Near field magnitude of the sensor array. (c) Reflection coefficient of each antennas. (d) Radiation pattern of the sensor array

From

Figure 4.8(b) and (c) we can conclude that the each antenna of the cubic shape sensor array has the ability to reach the same level of radiation power at the same time while also resonating at. However,

Figure 4.8(d) shows that the best radiation pattern actually happens when the angle theta equals 85 and 95 degrees. Which means the highest power is not concentrated at the tip of the antenna. Instead, it actually slightly shifted to the sides. This was also identified in FEKO simulation studies.

CHAPTER 5 BACKGROUND AND INTRODUCTION

The major research objectives of the project are:

- Simulate the pipe crack propagation using XFEM and investigate the effect material properties, pressure, and crack geometries to the final failure.
- Design of experiments and response surface method to construct a function between the load carrying capacity with respect to design variables.
- Perform probabilistic reliability analysis considering the uncertainties

About 65% of all failures in PE gas pipes are due to excavation damage. Outside of excavation damage, evaluations and laboratory analyses have shown that plastic polyethylene (PE) gas pipe materials fail by one of three modes. These modes are ductile rupture, brittle-like slow crack growth (SCG) failures, or rapid crack propagation (RCP) failures. The majority of plastic PE pipe in-field failures are typically the result of slow crack growth. About 1% of failures are ductile ruptures resulting from pipe over pressurization. Plastic pipes experience ductile rupture failures due to the presence of high internal pressures. For PE pipes, they occur as a result of increasing pressure to levels greater than 400psig. Increasing pressures cause the pipe to undergo large diametric expansions typically resulting in wall thinning and stretching until a point where the remaining wall ligament is not sufficiently large to withstand the induced high circumferential hoop stresses.

Plastic pipes experience ductile rupture failures due to the presence of high internal pressures. For PE pipes, they occur as a result of increasing pressure to levels greater than 400psig. Increasing pressures cause the pipe to undergo large diametric expansions typically resulting in wall thinning and stretching until a point where the remaining wall ligament is not sufficiently large to withstand the induced high circumferential hoop stresses.

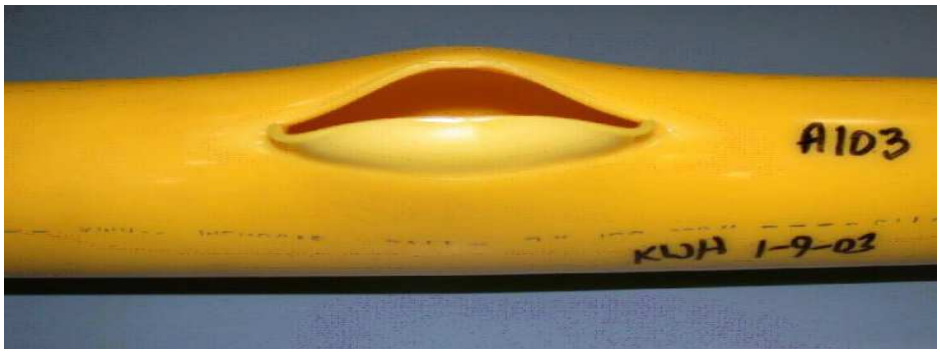

Figure 5.1 Ductile Failure Resulting From a Quick Burst Test[1]

Slow crack growth (SCG) failures occur over long periods of time at relatively low loads below the yield point of the material and are characterized by brittle (slit) fractures which exhibit very little material flow or deformation. Examinations show cracks initiate and radiate from an initiation point. Initiation points are stress risers caused by inclusions, contaminants, scratches, defects, cavities, dimples, high stress risers, etc. SCG failures grow stepwise and are associated with the sequential formation and fracture of the craze damage zone formed ahead of the crack tip.

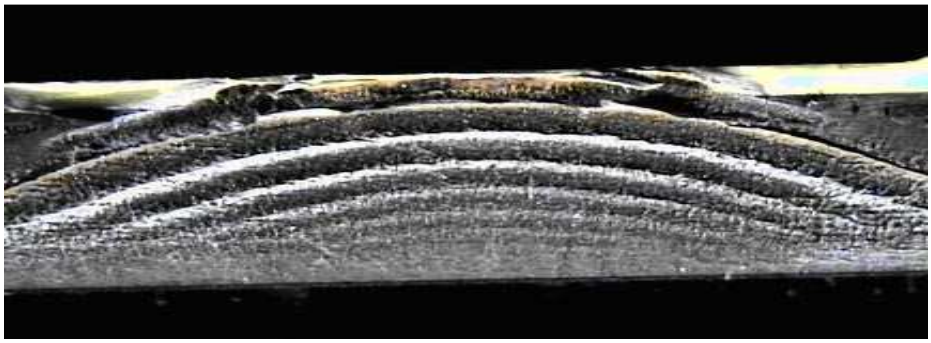

Figure 5.2 SCG Failure Morphology [1]

Rapid Crack Propagation (RCP) failures are manifested in the form of a large-scale brittle crack that propagates at high speeds exceeding 300 ft. /sec over a long span of polyethylene pipe. RCP failures could be catastrophic due the rapid release of high volumes of gas over long spans. In order for RCP to occur, a “critical” initial axial notch must exist in the pipe wall and the driving force has to exceed the dynamic fracture resistance of the material. The dynamic fracture resistance decreases with decreasing temperatures making PE materials more susceptible to RCP ruptures at lower field temperatures. The

susceptibility to RCP also increases with increasing field service pressure, increasing pipe diameter, increasing dimension ratio, SDR, and decreasing modulus of elasticity of the PE.

Figure 5.3 RCP rupture induced in a Small-Scale Steady State S-4 test [1]

There are four major types of failure which are associated with PA-11 pipelines: 1) Rock impingement induced cracking; 2) Force fracture of joints; 3) Improper squeezing induced failure; 4) Welding location leaking. Out of these, rock impingement was studied first as it is the most common type of field failure and occurs more frequently when compared to others. This report covers a parametric study of rock impingement type field failure and also simulation results of forced fracture.

Figure 5.4 Rock impingement

Figure 5.5 Force fracture of joints

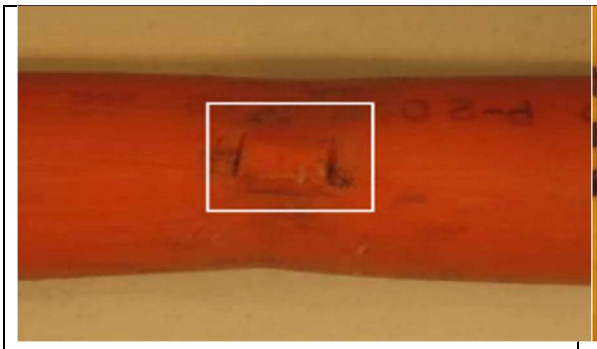

Figure 5.6 Improper squeezing

Figure 5.7 Welding location leaking

CHAPTER 6 NUMERICAL SIMULATION USING EXTENDED FINITE ELEMENT METHOD(XFEM) AND COHESIVE ZONE METHOD(CZM)

6.1. Overview and Objective

In Classical finite element method (FEM) adaptive meshing can be used for crack analysis, but it is very time consuming for large system analysis. Since objective is to develop optimized prognosis algorithms for efficient and accurate failure analysis and prediction XFEM is used. In FEM there are many methods to simulate crack propagation but due to high accuracy requirement and easy of computation we choose XFEM over FEM.

THE cohesive zone modeling (CZM) is gradual fracture phenomenon based on the separation of surfaces involved in cracking takes place in between material surfaces which is resisted by using cohesive tractions. The main advantage of this method is it has no stress singularity at crack tip. Unlike conventional methods, size of non-linear zone around crack tip does not have to be negligible and it can also predict behavior of un-cracked structures.

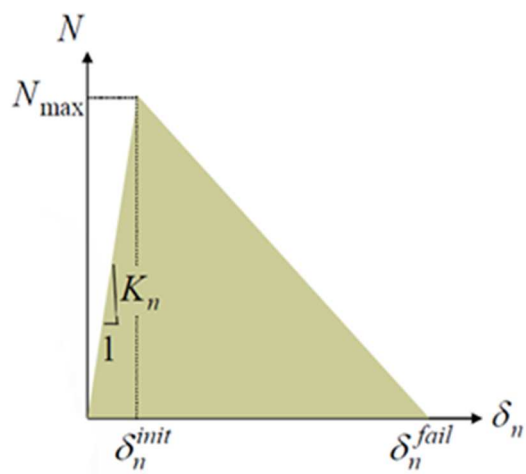

N_{max}= maximum principal stress
δ_n^{fail} = strain at failure

Figure 6.1 Schematic illustration of the traction separation law in CZM

The advantages of using XFEM and CZM technique are: 1) The use of CZM will enable the predictions under complex loading conditions and for different failure modes; 2) XFEM allows the non-matching mesh with respect to the crack and allows the arbitrary tracking of the CZM within the simulation domain.

From previous literatures, numerical methods such as virtual crack closure technique (VCCT), cohesive zone model (CZM) and extended finite element method (XFEM) are

widely used to simulate fracture problems. Bouvard and Siegmund [2, 3] applied cohesive zone theory to predict crack initiation and propagation. Fawaz and Zhang [4, 5] exerted VCCT to study crack propagation of composite structures. However, both of these two methods have their intrinsic limitation. Classical cohesive zone model needs to know the crack path before simulation. Also, the remeshing process during crack propagation is very time consuming in these two methods. So as to overcome these shortcomings, many researchers [6, 7] applied XFEM to simulation fracture problem. This method can simulate arbitrary crack propagation without remeshing. Also, it can predict crack initiation and propagation for both brittle and ductile materials.

Two ingredients of failure mechanism in XFEM are crucial: a damage initiation criterion and a damage evolution law. In our simulation, the maximum principal stress criterion is used for damage initiation and the exponential response is used for damage evolution. During XFEM simulation in ABAQUS, as internal pressure increases in each step, the principal stress of elements near the real crack tip increases. When principal stress reaches maximum principal stress, the damage first occurs. Then a cohesive crack appears and starts propagation long axial and depth direction crossing through inner damaged elements. Once the energy release rate at cohesive crack tip reaches the critical value, the cohesive crack will becomes real crack. When the maximum crack size reaches the critical value, the pipe is considered failure.

6.2. Impingement failure simulation under static loading

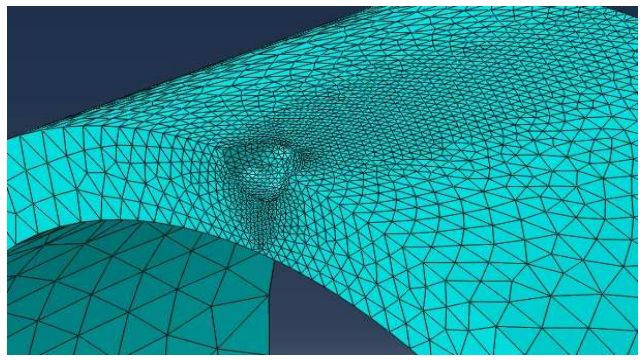

a) b)

Figure 6.2 Geometry and meshing of the pipe model

In this example, only one-half geometry is modeled computational efficiency (Figure 6.2 (a)). A cavity on top of the pipe is inserted to simulate the dent due to impingement. The model was meshed using various control parameters such as imprinting faces, edge biasing, edge divisions etc. to achieve good quality elements in the desired region. Tet elements were used as body had a curved surface. After meshing, material model was assigned. A bilinear isotropic plasticity model was incorporated. The parameter's values chosen to define the model are as under.

- Mod. of Elasticity – 1700 MPa
- Poisson's Ratio – 0.4
- Tensile Strength, Ultimate – 68.9 MPa
- Tensile Strength, Yield – 44 MPa
- Tangent Mod. – 2.5% of Mod. of Elasticity
- CZM, Criterion – Max. Principal Stress
- CZM, Peak Value – 52 MPa
- CZM, Damage Evolution – Energy, Exponential Softening
- CZM, Fracture Energy – 620 KJ/m^2

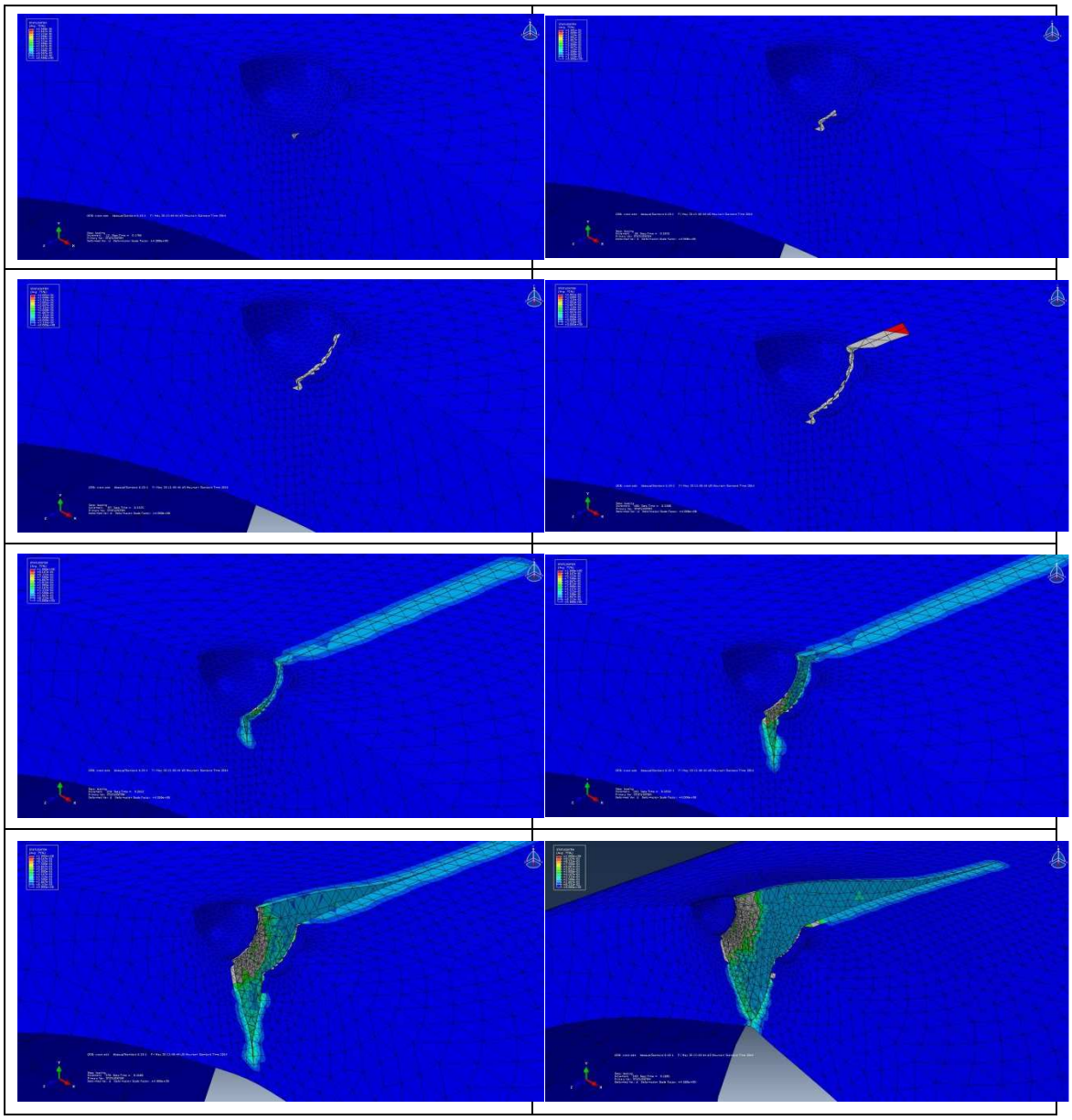

Figure 6.3 Crack Propagation

Static failure and crack propagation with increased internal pressure is simulated and the results are shown in Figure 6.3 for the cracking. It is observed that the crack initiates as the loading increases. The crack propagates along the pipe longitudinal direction until the final unstable fracture. Von-mises stress plots around the crack are attached below.

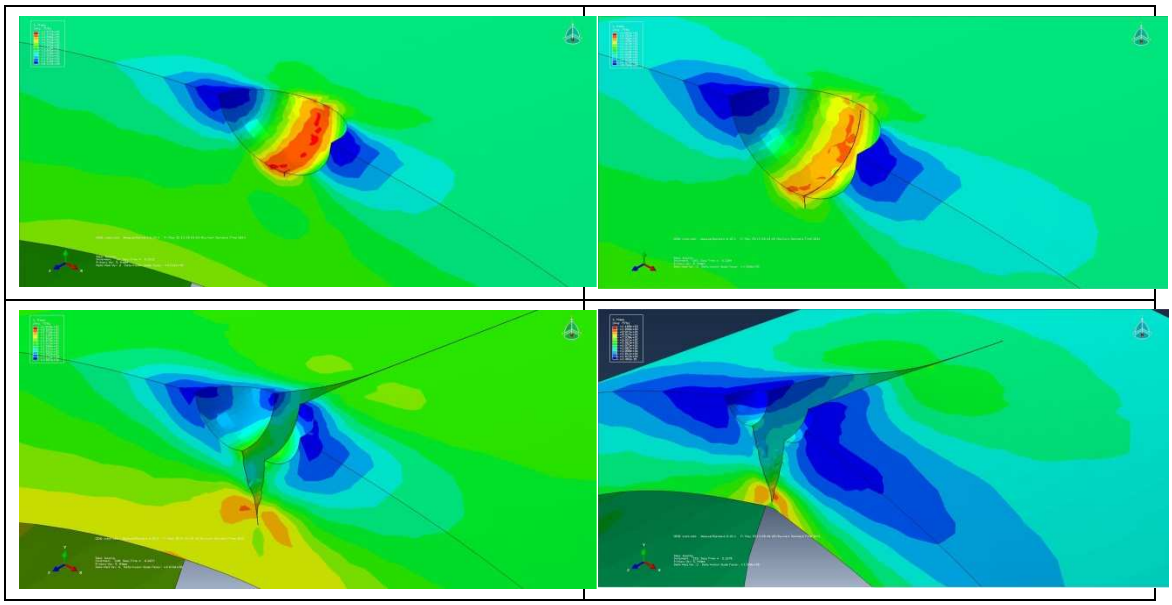

Figure 6.4 Von – mises Stress Plots

Detailed parametric studies were carried out by considering three major parameters: internal diameter; pipe Thickness, and cavity size. These parameters were varied individually while keeping others constant to understand the impact of that particular parameter under analysis. The internal diameter was varied over a range to understand its impact on the critical pressure (Pc – the pressure when the unstable crack occurs/the crack penetrates the thickness). The results are shown in Figure 6.5. As expected the critical pressure decreases as the internal diameter increases. The trend is not linear as the reduction rate for smaller diameter pipe is faster. Pc is observed to decrease as the pipe thickness decreases in almost linear fashion. Pc decreases as the cavity size increases. The parametric study results are shown in Figure 6.5.

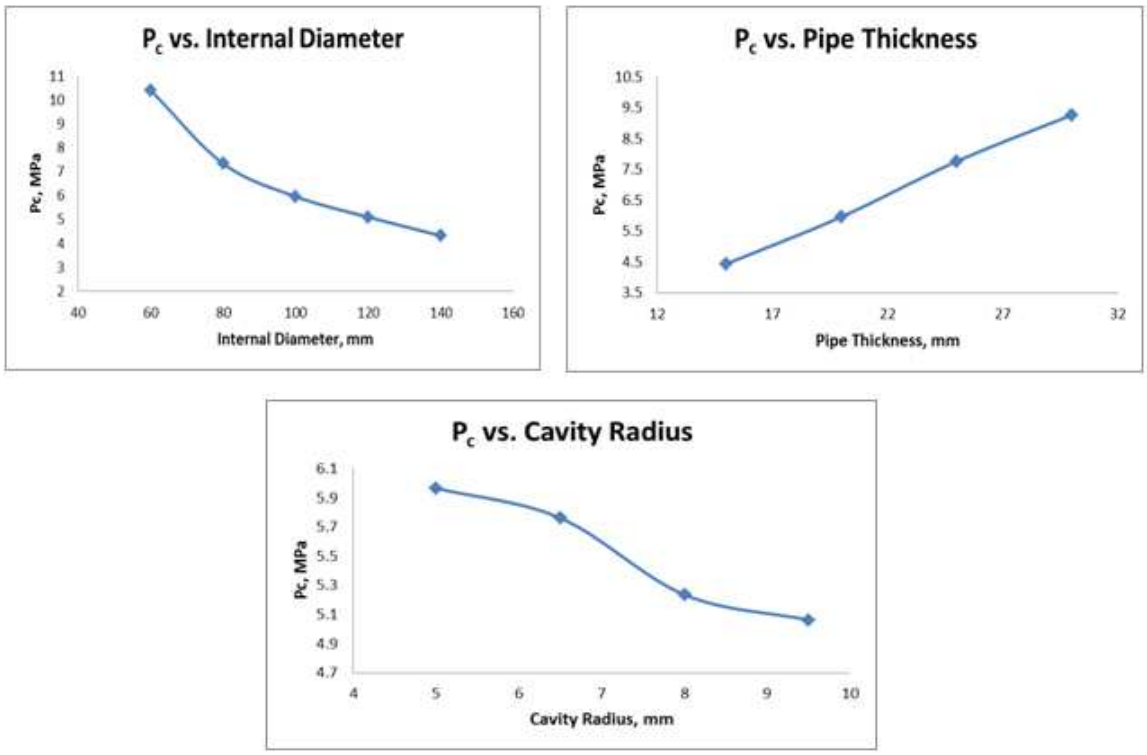

Figure 6.5 Parametric study for static failure due to impingement

6.3. Impingement failure simulation under static loading

The process flow is same as that of Rock impingement type failure. Here, a T-joint was modeled to observe how it cracks under applied force. After modeling the geometry, mesh was assigned. Again various methods were adopted to get a good quality mesh. After assigning the mesh, material model was given. Same material model was used as T-joint was made from same material. The upper and lower faces of the longitudinal (main) pipe were fixed and force/displacement was applied at the end of lateral pipe.

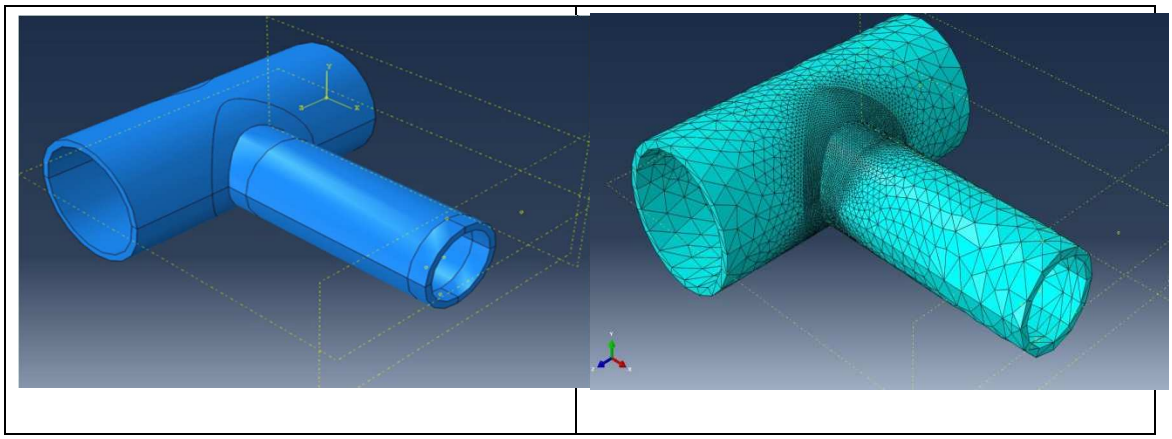

Figure 6.6 Geometry and meshing of the T joint

The force fracture failure is simulated with a tip load at the T joint. Due to the large bending stress, the failure happens at the intersection root of the T joint. One major cracks appears on the surface followed by several secondary cracks near the major crack. The final fracture happens as the coalesce of the several cracks. The simulated fracture process is shown in Figure 6.7.

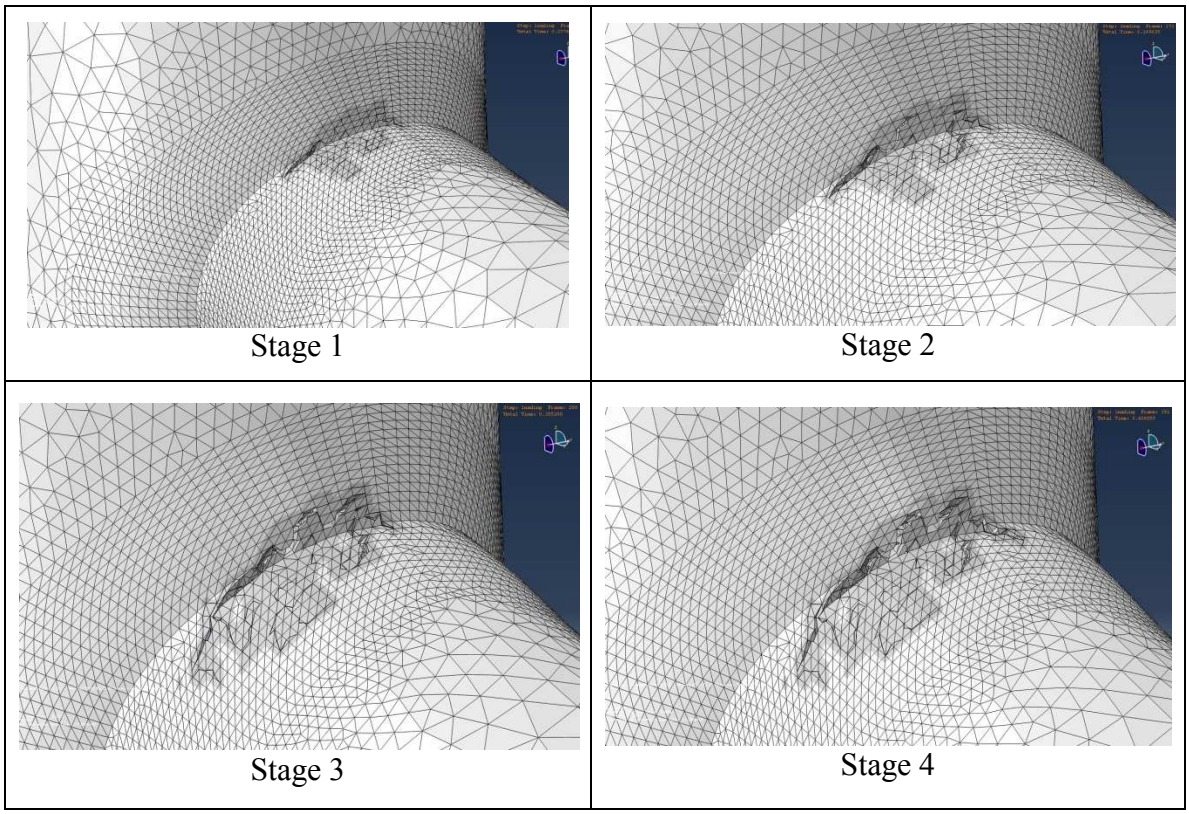

Figure 6.7 Simulated force fracture at a T joint

6.4. Slow crack growth due to creep and impingement loading

In this part of report, a methodology is defined on how to simulate Slow Crack Growth under creep with given loading conditions. This investigation focuses on the time dependent failure of pipeline structures. As done earlier in all simulations, XFEM and cohesive zone model was also used. The challenge in this kind of simulation was to achieve coupled behavior that being cracks initiation and propagation dominated by creep model. This methodology is adopted for two kinds of universal specimens and then later incorporated into the pipe model.

Mechanical properties of polymers vary enormously with time and temperature. The time dependence complicates measurement of these properties since specific conditions under which experiments are carried out must necessarily be incorporated into the definition of appropriate parameters. Thus, the terms creep, stress relaxation and dynamic mechanical measurements are all common in this field [8]. The mechanical properties of a polymeric component are dominated by its viscoelasticity. This is reflected by the time-dependency of the mechanical response of a component during loading. Hence, a polymer behaves differently if subjected to short term or long term loads [9]. A brief review for the fundamental creep mechanics is briefly mentioned below.

A polymer, at a specific temperature and molecular weight, may behave as a liquid or a solid, depending on the speed (time scale) at which its molecules deform. This behavior, which ranges between liquid and solid, is generally referred to as the viscoelastic behavior or material response. Polymers are viscoelastic materials and exhibit time-dependent relaxations when subjected to stress or strain. While creep is a measure of increase in strain with time under a constant stress, stress relaxation is the reduction of stress with time under a constant strain. Therefore, creep and stress relaxation tests measure the dimensional stability of a polymer over time. Such tests are of great importance for investigated materials, particularly if a polymer must be in service under stress and strain for long periods [10]. This report is limited to linear viscoelasticity, which is valid for polymer systems undergoing small or slow deformations. Non-linear viscoelasticity is required when modeling large rapid deformations, such as those encountered in flowing polymer melts. In linear viscoelasticity, the stress relaxation test is often used, along with the time

temperature superposition principle and the Boltzmann superposition principle, to explain the behavior of polymeric materials during deformation [9].

When a plastic material is subjected to a constant load, it deforms continuously. The initial strain is roughly predicted by its stress-strain modulus. The material will continue to deform slowly with time indefinitely or until rupture or yielding causes failure. The primary region is the early stage of loading when the creep rate decreases rapidly with time. Then it reaches a steady state which is called the secondary creep stage followed by a rapid increase (tertiary stage) and fracture (Figure 6.8).

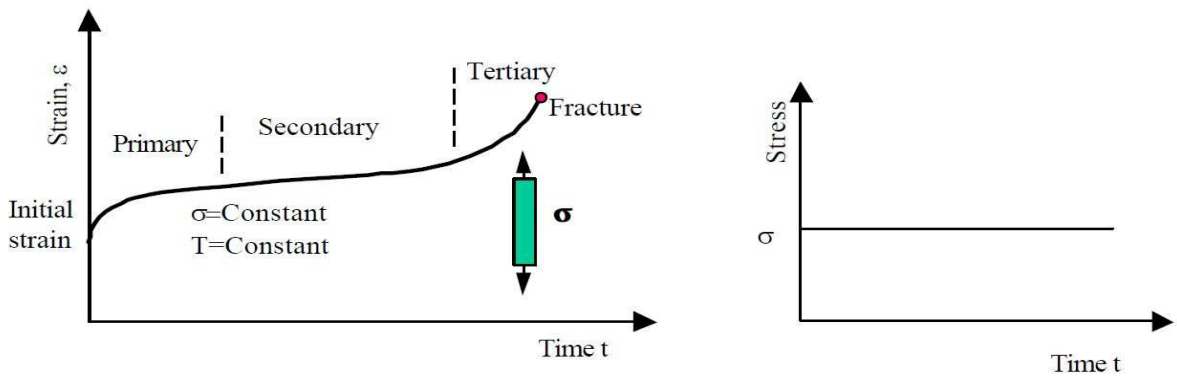

Figure 6.8 Schematic illustration of creep behavior [11]

If the applied load is released before the creep rupture occurs, an immediate elastic recovery equal to the elastic deformation, followed by a period of slow recovery is observed (Figure 6.9). The material in most cases does not recover to the original shape and a permanent deformation remains. The magnitude of the permanent deformation depends on length of time, amount of stress applied, and temperature [12].

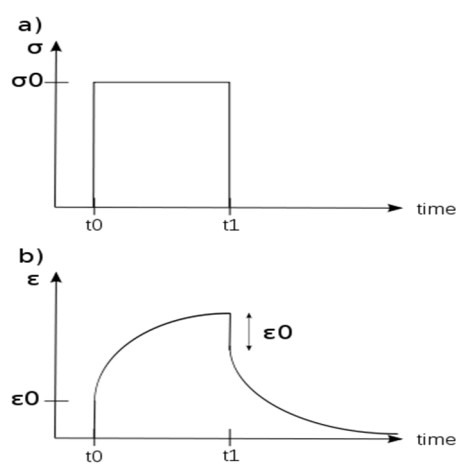

Figure 6.9 Schematic illustration of strain recovery [11]

The most commonly used mechanical test is the short-term stress-strain tensile test. For comparison, the figure also presents stress-strain curves for copper and steel. Although they have much lower tensile strengths, many engineering polymers exhibit much higher strains at break than metals. The next two sections discuss the short-term tensile test for cross-linked elastomers and thermoplastic polymers separately [9].

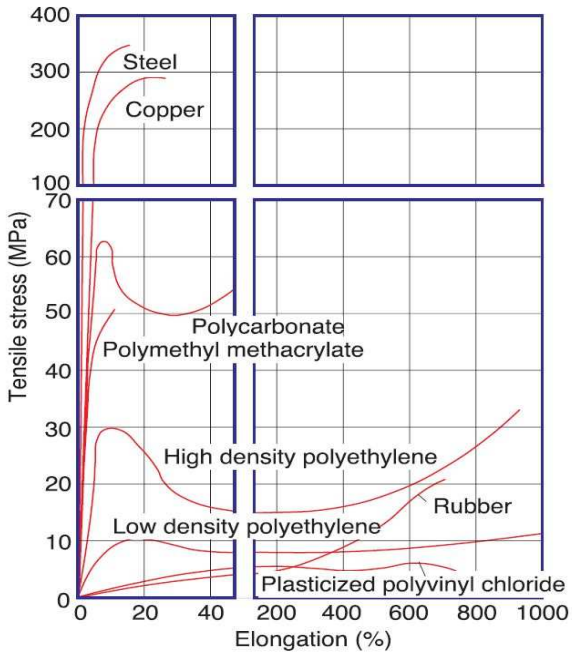

Figure 6.10 Typical tensile stress-strain curves for several materials [9]

The stress relaxation and the creep test are well-known long-term tests. The stress relaxation test is difficult to perform and is, therefore, often approximated by data acquired through the more commonly used creep test. The stress relaxation of a polymer is often considered the inverse of creep. The creep test, which can be performed either in shear, compression, or tension, measures the flow of a polymer component under a constant load. It is a common test that measures the strain, ε, as a function of stress, time, and temperature. Standard creep tests such as DIN 53 444 and ASTM D2990 can be used. Creep tests are performed at a constant temperature, using a range of applied stress. If plotting creep data in a log-log graph, in the majority of the cases, the creep curves reduce to straight lines. Hence, the creep behavior of most polymers can be approximated using a power law with time [9, 12]as

$$\varepsilon_t = k(T)\sigma^m t^n \qquad (6.1)$$

where k(T), m and n are material dependent properties, T is the temperature

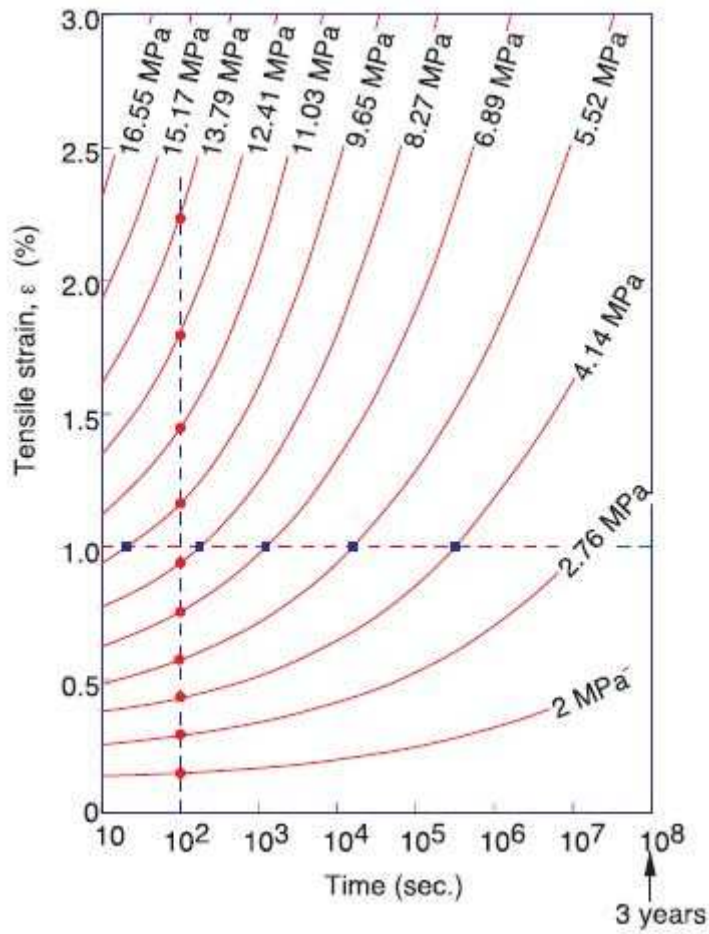

Figure 6.11 Creep response of a propylene-ethylene copolymer at 20 °C [9]

Modeling and simulation were carried out in ABAQUS software as it gave the freedom of using XFEM and CZM technique. Several case studies are performed below to check suitability of proposed method.

A plate with double edge notch specimen under uniaxial tension is used in this case. The material properties are:

- Mod. of Elasticity – 1700 MPa
- Poisson's Ratio – 0.4
- Creep Power Law Multiplier – 3.125E-10
- Creep Stress exponent, m – 5

- Time order, n – 0
- Dimensionless time period – 30
- Creep tolerance – 0.005

The geometry, mesh and boundary conditions are shown below.

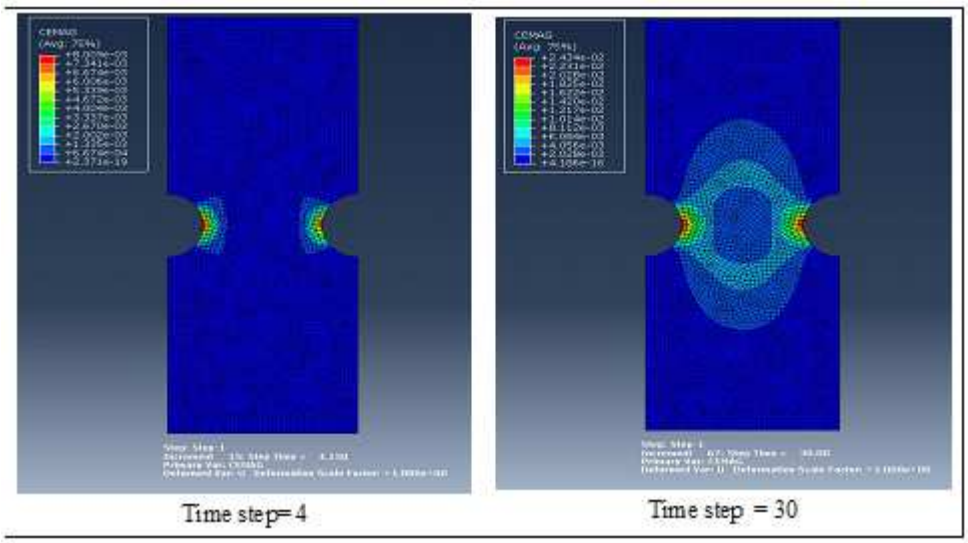

Figure 6.12 Simulation results at different time steps

After the creep simulation is successfully done. The XFEM and CZM are added for the time dependent fracture simulation. The following material model was used to simulate creep, XFEM, CZM, crack initiation and propagation. Similar geometry with 3D finite element is used in this case and corresponding geometry, mesh and boundary conditions are shown in Figure 6.13. The simulation results are shown in Figure 6.14. It is shown that the creep induced crack appears at the notch root as time increases and will propagate perpendicular to the loading direction.

- CZM, Criterion – Max. Principal Stress
- CZM, Value – 30 MPa
- CZM, Damage Evolution – Energy, Exponential Softening
- CZM, Fracture Energy – 300 KJ/m2
- CZM, Damage Stabilization Cohesive – 0.005
- Time period – 50

- Creep tolerance – 0.0005

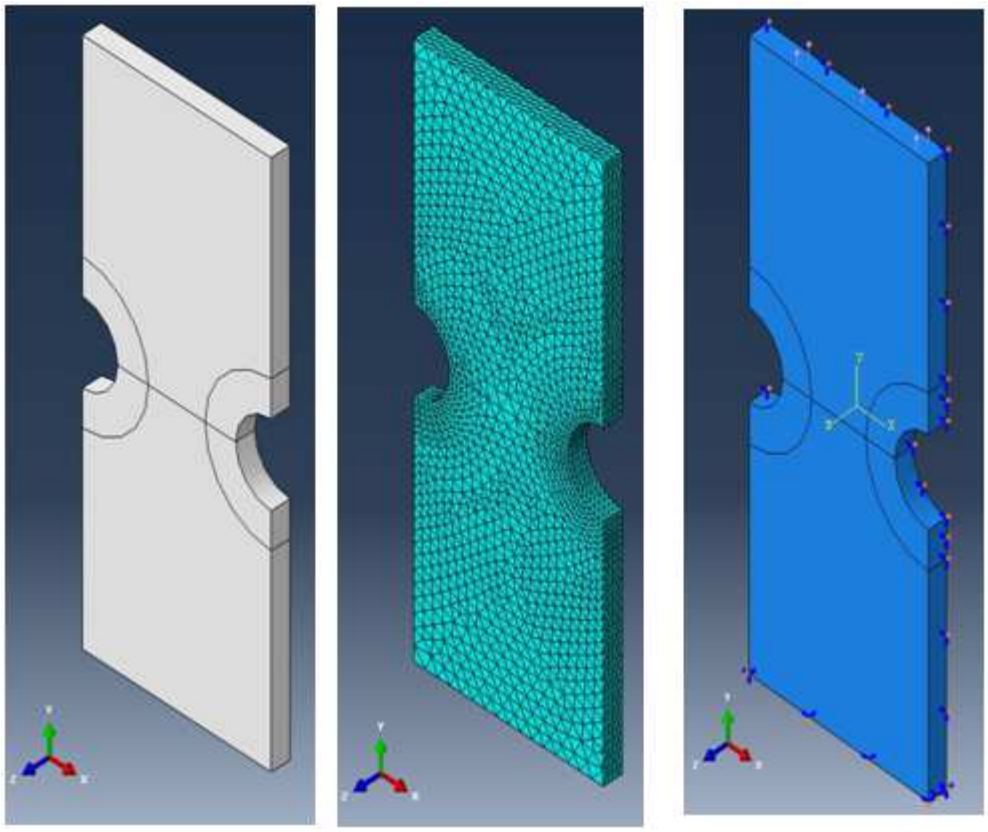

Geometry Mesh BC and loading

Figure 6.13 Model setup for notched plate model

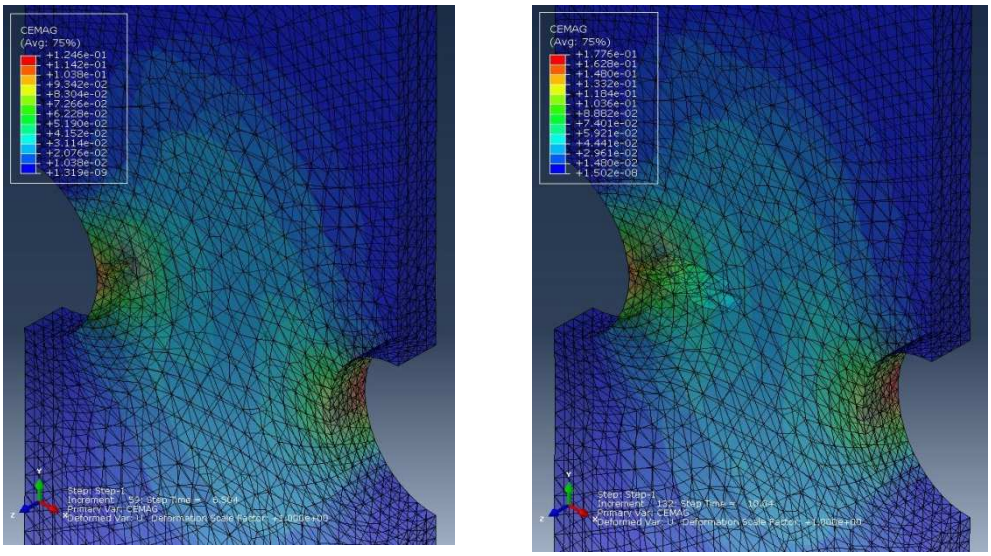

Time step 6 **Time step 10**

Figure 6.14 Simulation results at different time step

The similar technique was applied for pipe failure simulation. In this example, the impingement dent will be simulated as the creep information is included. No artificial cavity is introduced in the pipe model and the difference in geometry can be observed in following figures. The cavity was formed due to application of pressure. This is equivalent to a rock particle applying pressure on pipe. Along with geometry some parameters in material model were also tuned to get the desired results. Tuned values of material parameters are listed below.

- Mod. of Elasticity – 1700 MPa
- Poisson's Ratio – 0.4
- Creep Power Law Multiplier – 2.15E-9
- Creep Stress exponent, m – 6.5
- Time order, n – 0
- Dimensionless time period – 70
- Creep tolerance – 0.00001

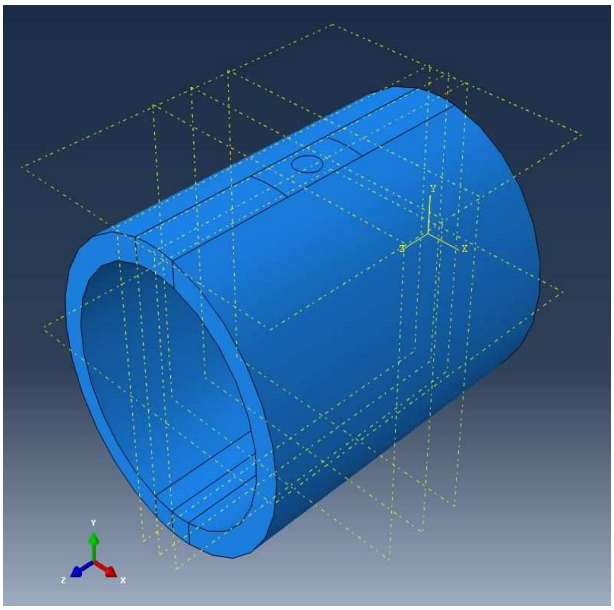

Figure 6.15 Model for the creep analysis

As seen, the new model does not have in built cavity. Instead it has a circular face on which pressure will be applied. Apart from modification in cavity region, the new model was lengthier as it can be observed in the figure. Due to different boundary conditions it

became mandatory to increase the length of the pipe. The planes seen in new model (Figure 6.15) are datum planes that were used to impart a better quality mesh and better assignment of XFEM and CZM to the pipe. XFEM property was assigned to narrow center part seen on top of the surface. This defines the path for crack and helps in controlling the simulation.

To reduce the number of mesh elements several surfaces were imprinted on the geometry. After imprinting and seeding the edges, following mesh was created.

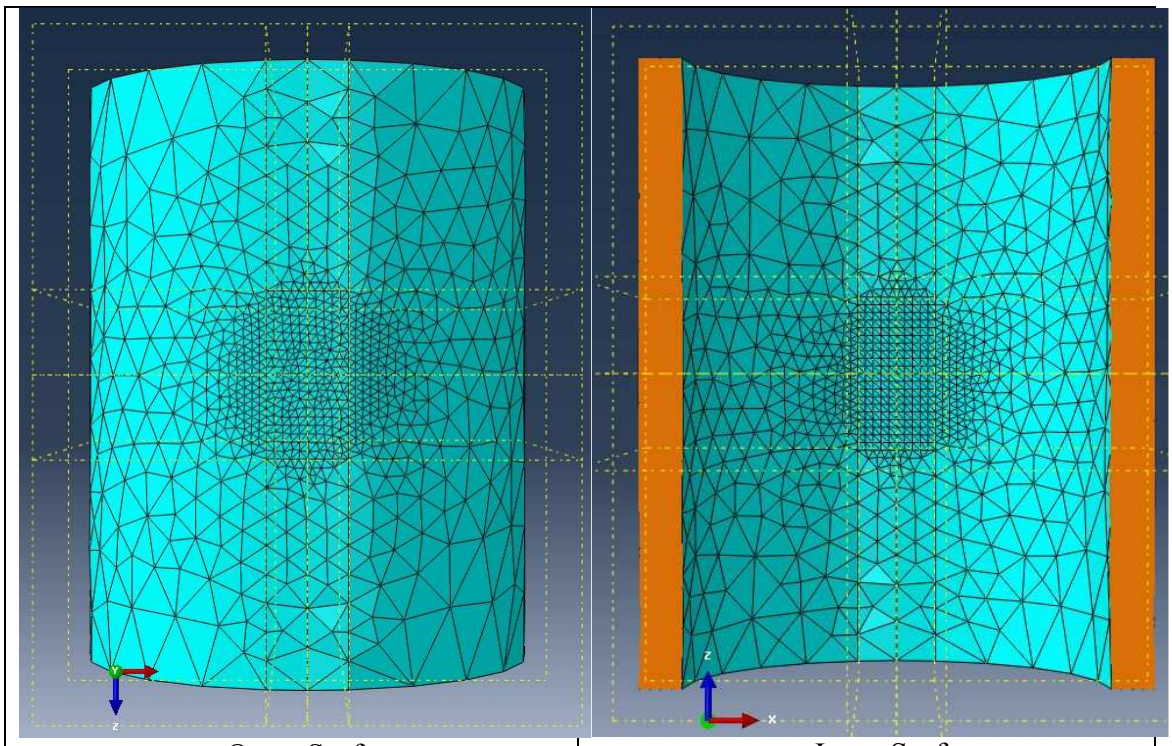

Outer Surface	Inner Surface

Figure 6.16 Mesh near the impingement location at the outer and inner surfaces

Following rules were considered for giving boundary conditions

- BCs can only be applied in directions that the element has degrees of freedom.
- Every degree of freedom must be restrained in at least one place in the model.
- There must be at least one applied load to get a solution.

Following loading conditions were applied:

- Internal pressure of 0.5 MPa

- Rock particle pressure of 3 MPa on the imprinted circle representing the location of the cavity.

The simulation results are shown in Figure 6.17. It is shown that the pipe cracks due to creep model used and hence produces a creep dominated crack. Since a pressure is applied by a rock particle, a cavity forms at the same location. The crack first occurs at the inner surface due to the local bending caused by the impingement. The crack will propagate along the longitudinal direction of the pipe. The final crack is defined as the thorough thickness crack or the crack propagation is not stable. The time unit used in Figure 6.17 is normalized time and 1 time unit indicates 365x24 hours (i.e., hours for one year). Thus, the crack length vs. time for the creep crack growth can be obtained from the numerical simulation. In the example in Figure 6.17, the final failure happens at 45.5 years.

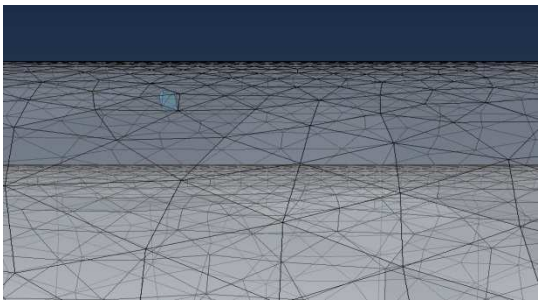

Crack initiation at inner surface

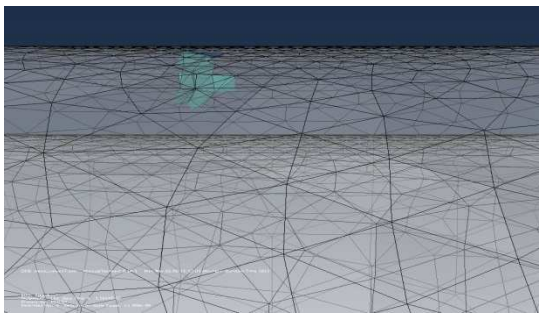

Crack propagation at time 4.6

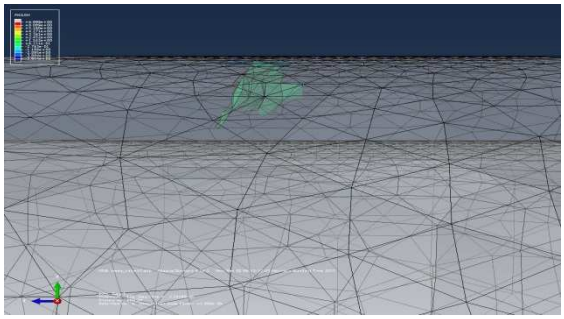

Crack propagation at time = 29.5

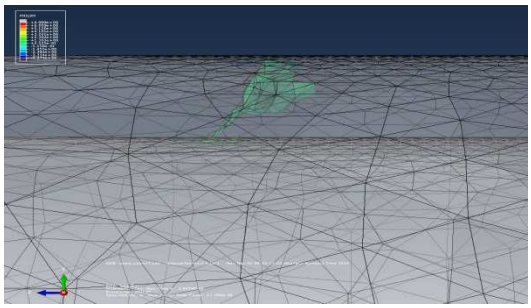

Crack propagation at time = 45.5

Figure 6.17 Simulation results of slow crack propagation

CHAPTER 7 PROBABILISTIC PROGNOSIS ANALYSIS

7.1. Overview and Objective

Generally, probabilistic analysis always requires a large number of evaluations of system response, which are intractable if the system of response is generated from finite element simulation. The idea of the surrogate model is to choose appropriate explanatory variables that can describe certain aspects of systems, in which the sensitivity analysis can be used for selecting the variables that have high impact on the system response [13, 14]. Design of experiments are widely used for generating samples that can uniformly cover the whole domain of the explanatory variables[15, 16]. In order to accurately capture the system characteristics, a full factorial approach is necessary to investigate all possible combinations. However, it is infeasible to do the full factorial design for high dimensional problems. Latin hypercube design is considered as an optimal method for high dimensional experimental design, because every variable can be represented identically no matter how many samples are selected [17]. In this study, five variables are chosen to investigate the system response based on the numerical investigation. Latin hypercube sampling is employed to generate multiple combinations (i.e. DoE) of design variables. The corresponding system response of each DoE can be computed using the developed finite element model. With these samples, a surrogate model that can capture this system behavior is developed, which makes it possible for probabilistic analysis with respect to each design variable using Bayesian updating.

7.2. Design of Experiments and Surrogate Model Development

The Latin hypercube sampling (LHS) is very flexible to be used to create any number of design of experiments. A lot of work has been done on the optimization of Latin hypercube from both optimization algorithm and objective criteria [18-21].

An experiment design with N point in D dimension is given as $X = [x_1, x_2, \dots x_N]^T$, in which each column represents a random variable and each row x_i represents a realization. A Latin hypercube design is performed in such a way that each dimension is divided into N equally probable intervals and there is only one sample within each interval. In this study, a criteria with maximizing the minimum distance is implemented to generate Latin

hypercube samples. Five random variables are chosen and the corresponding sampling interval for each variable is listed in Table 7.1 .

Table 7.1 Sampling interval for each random variable

Random variable	Creep constant (Mpa/s)	Fracture Energy (MJ/mm^2)	n	Principal stress (Mpa)	Load (Mpa)
Mean	2.15×10^{-3}	0.620	6.5	51	25
Sampling interval	$[1.15,3.25]\times 10^{-3}$	[0.590, 0.650]	[4.5,8.5]	[46,56]	[15,35]

Using Latin hypercube sampling method, 20 design of experiments are generated, which are listed in Table 7.2. The projection of these samples on each 2D plane is given in Figure 7.1.

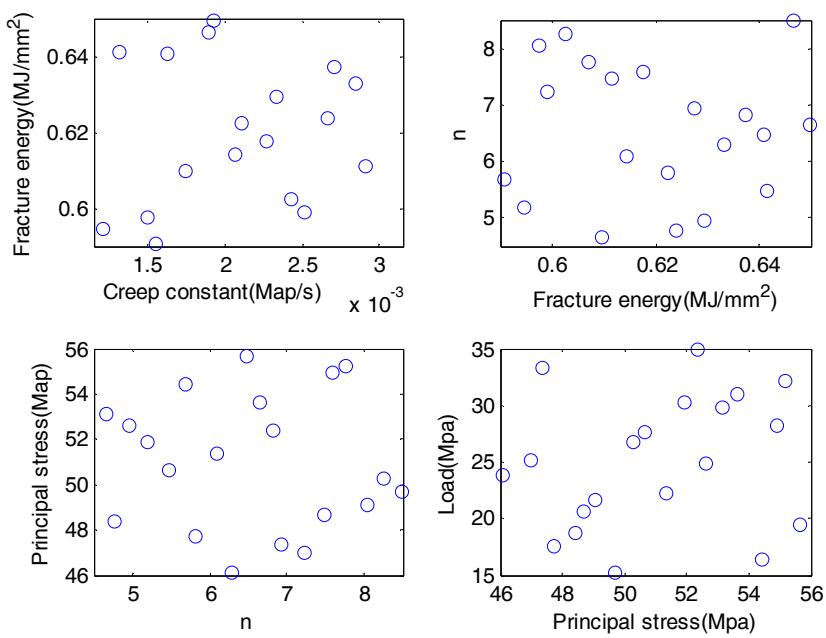

Figure 7.1 The project of 20 samples on each 2D plane

For each DoE, the system response such as crack length vs. time curve can be generated using the FEM model developed above. During simulation, some cases may crash because of impractical variable combination is input into the FEM model. By ignoring them, crack growth curves for 8 DoEs are plotted in Figure 7.2.

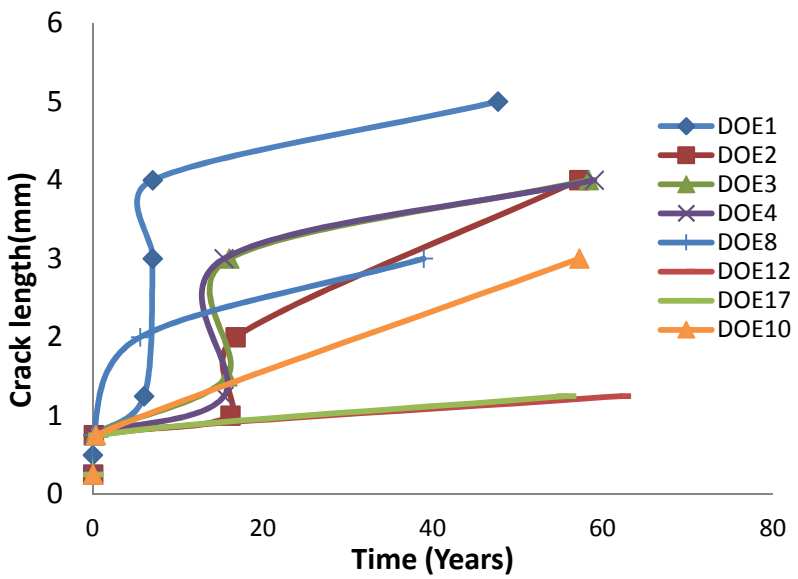

Figure 7.2 The crack growth curves for 8 DoEs

Table 7.2 The 20 DoE samples generated using LHS

S.No	A (e-3)	Frac Energy(e-3)	n	principal stress	Load
1	1.625218	640.9721293	6.477983	55.67172305	19.40992
2	2.702999	637.4050148	6.831243	52.36128171	34.99771
3	1.930486	649.9379596	6.647187	53.64543485	31.05547
4	2.272673	617.6231862	7.583964	54.93485224	28.20752
5	2.104886	622.4275118	5.812922	47.73800136	17.60067
6	2.509233	599.1437521	7.21698	46.97705494	25.12655
7	1.554258	590.6893212	5.689157	54.44934716	16.3256
8	2.426683	602.5502794	8.248061	50.26553246	26.75763
9	1.744176	609.7218497	4.651164	53.14467682	29.83156
10	1.100611	607.0993455	7.758181	55.1993268	32.13888
11	2.66107	623.9591286	4.76823	48.39754151	18.67336
12	2.911832	611.424453	7.476164	48.69060674	20.67485
13	1.310673	641.3846212	5.474156	50.65042494	27.59983
14	2.0614	614.3088125	6.084406	51.34258566	22.23649
15	2.327245	629.4692397	4.952952	52.59760568	24.83593
16	1.208735	594.5445463	5.18877	51.91098878	30.31171
17	1.009587	627.5343785	6.933126	47.37934714	33.35668
18	1.891855	646.8039981	8.478775	49.70263502	15.17865
19	1.496666	597.6290569	8.048688	49.06588354	21.62145
20	2.842759	633.2133341	6.289175	46.09066581	23.8881

Conceptually, the developed surrogate model should be a time dependent model that has design variables as input parameters. However, it is not that straight forward to get this model in one step. The idea in this study is to fit the crack length with respect to time relationship using power law, and then the effect of design variables is incorporated in the model coefficients using other regression methods. Bearing this idea in mind, the proposed surrogate model is expressed as

$$\boldsymbol{a} = \boldsymbol{f_1}(\boldsymbol{P})\boldsymbol{t}^{\boldsymbol{f_2}(\boldsymbol{P})} + \boldsymbol{f_3}(\boldsymbol{P}) \qquad (7.1)$$

where t is the creep time and $f_1(P) = \alpha_0 + \alpha_i p_i$, $f_2(P) = \beta_0 + \beta_i p_i$, $f_3(P) = \gamma_0 + \gamma_i p_i$, in which p_i represents the design variables. After fitting this model, the true and predicted crack length vs. time data are illustrated in Figure 7.3. In order to investigate the model sensitivity respect to each design variable, the crack length variation due to 10% perturbation of each design variable at creep time $t = 10$ years is demonstrated in Figure 7.4.

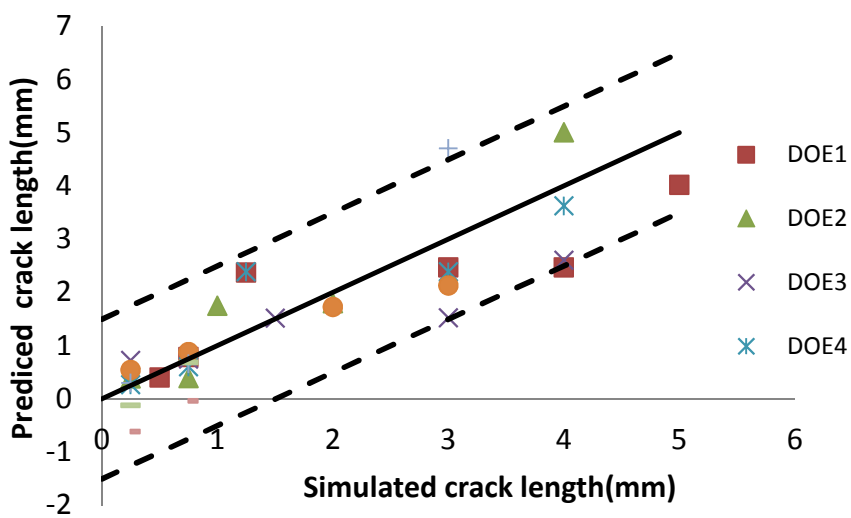

Figure 7.3 The comparison between true and predicted crack length

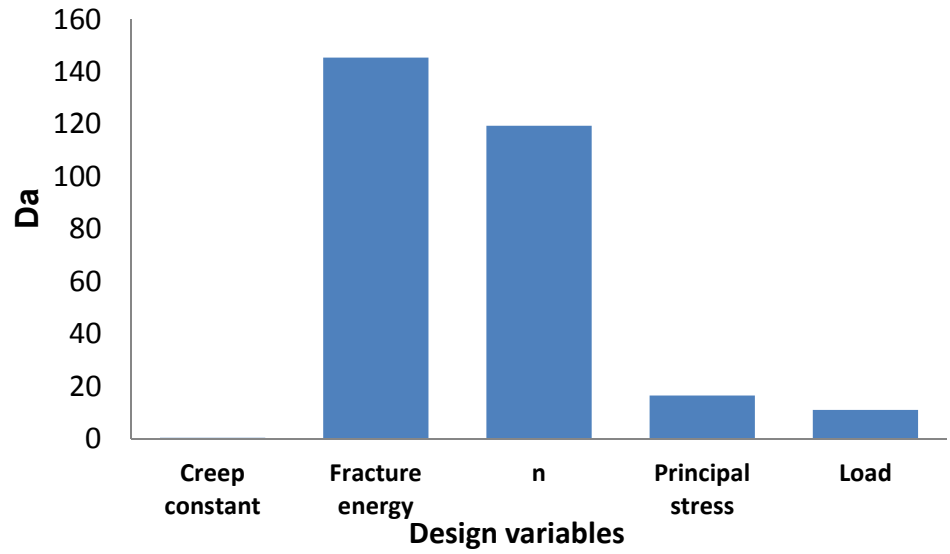

Figure 7.4 The crack length variation for the perturbation of each design variable

As seen in Figure 7.3, the proposed model can generally capture the crack growth trend for different DoE samples, but there are relatively large uncertainties embedded in the prediction. Based on this model, it can be concluded that the crack growth is more sensitive to the parameters that control the crack initiation and material creep behavior, which is given as the fracture energy and *n* in Figure 7.4.

7.3. Uncertainties Reduction using Bayesian Updateing

Bayes' theorem is commonly used for probabilistic inference or learning process. It combines prior belief about system/process parameters and current system response to provide a reasonable estimate of current parameters distribution. Let $\mathrm{p}(\theta)$ denote the prior distribution of parameters θ in a model $\mathrm{M}(\theta)$. Assume $\theta = [p_1, p_2, p_3, p_4, p_5]$, the posterior distribution of θ is given as

$$\mathrm{q}(\theta) \propto \mathrm{p}(\theta)\mathrm{p}(\mathrm{x}'|\theta) \tag{7.2}$$

where $\mathrm{p}(x'|\theta)$ is the likelihood function, which reflects the measured crack length x' given parameters θ, and $\mathrm{q}(\theta)$ is the posterior distribution of updated parameters. In our formulation, x' is the synthetic crack length measurements. If there is no measurement noise or model uncertainty present, the measurements would be identical to the model

prediction, i.e. $x' = \mathrm{M}(\theta)$. However, this is usually never the case. Therefore, it is necessary to account for measurement noise ϵ in the estimation. In our formulation, the relationship between x' and $\mathrm{M}(\theta)$ is expressed as

$$\mathrm{x}' = \mathrm{M}(\theta) + \epsilon \tag{7.3}$$

Assuming that the error term ϵ is the zero mean normal variable noise [22, 23], the distribution of this term can be expressed as a random variable $\epsilon \sim \mathrm{N}(0, \sigma_\epsilon)$. Therefore the likelihood function $\mathrm{p}(x'|\theta)$ can be expressed as

$$p(x_1', x_2', \dots x_n'|\theta) = \frac{1}{(\sqrt{2\pi}\sigma_\epsilon)^n} exp\left(-\frac{1}{2}\sum_{i=1}^{n}\left(\frac{(x_i' - M(\theta))}{\sigma_\epsilon}\right)^2\right) \tag{7.4}$$

where n is the number of available measurements. Substituting Eq.(7.4) into Eq.(7.2), the posterior distribution of parameter θ can be expressed as

$$p(\theta|x_1', x_2', \dots x_n') \propto$$
$$p(\theta)\frac{1}{(\sqrt{2\pi}\sigma_\epsilon)^n} exp\left(-\frac{1}{2}\sum_{i=1}^{n}\left(\frac{(x_i' - M(\theta))}{\sigma_\epsilon}\right)^2\right) \tag{7.5}$$

Then the posterior distribution of the parameter θ can be approximated by the samples drawn by the Markov Chain Monte Carlo (MCMC) simulation. Detailed discussion on MCMC method can be found in many references [24-27] and is, therefore, not discussed here.

With the help of the surrogate model developed above, the finite element simulation can be avoided when doing probabilistic analysis. To demonstrate the framework for uncertainties reduction, the synthetic measurements generated from a finite element simulation is incorporated in the Bayesian updating for parameters updating. Prior updating the parameters distribution, the prior distributions for these five design variables are given in Table 7.3. Using them, the prior belief of the crack growth curve is shown in Figure 7.5. Blue line represents the median prediction using the prior distribution of input parameters. Green line is the simulated crack growth curve. Red star represents the synthetic measurements based on the simulation.

Table 7.3 Prior distribution of these five design variables

Random variable	Creep constant (Mpa/s)	Fracture Energy (MJ/mm^2)	n	Principal stress (Mpa)	Load (Mpa)
PDF	Normal	Normal	Normal	Normal	Normal
μ	2.15	0.62	0.0065	51	25
σ	0.5	0.015	0.001	2.5	5

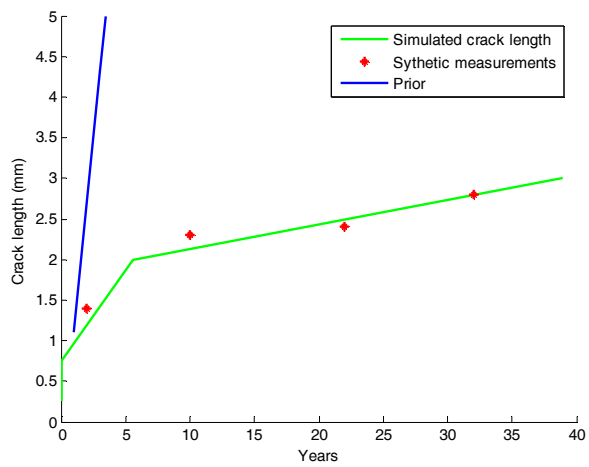

Figure 7.5 The prior belief of the crack growth curve

Given the prior distribution and the synthetic measurements, the posterior distribution of model parameters can be updated using the Bayesian theorem discussed Eq.(7.2)-(7.5) . Therefore, the updated posterior crack growth prediction is shown in Figure 7.6.

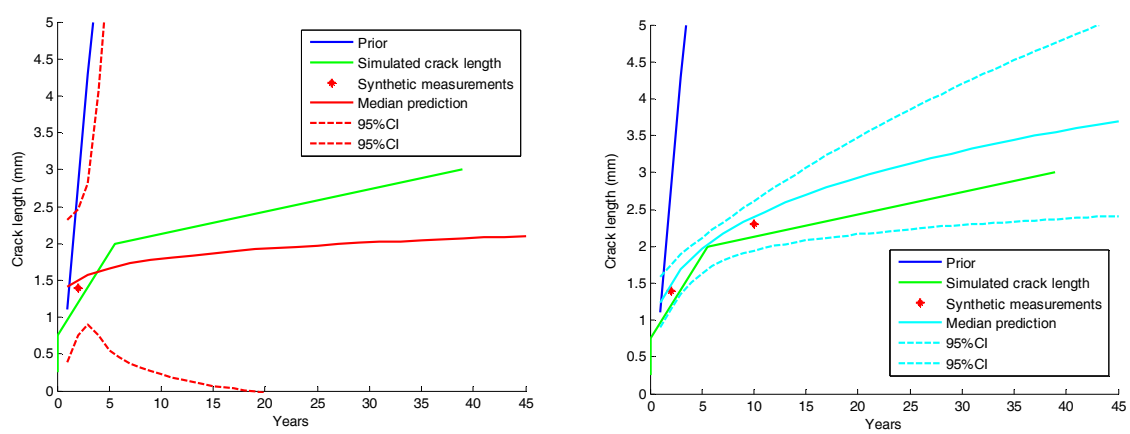

(a) (b)

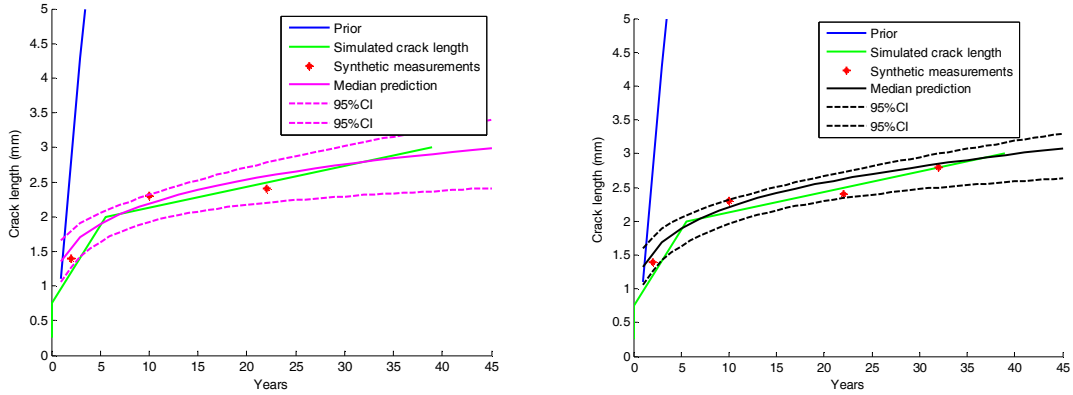

(c) (d)

Figure 7.6 The updated crack growth curves (a), Updating 1. (b), Updating 2. (c), Updating 3. (d), Updating 4.

As seen above, the 95% confidence interval (CI) is shrinking as more and more synthetic measurements are incorporated in the Bayesian updating. That can also be visualized and substantiated through the posterior distribution of design variables given in Figure 7.7.

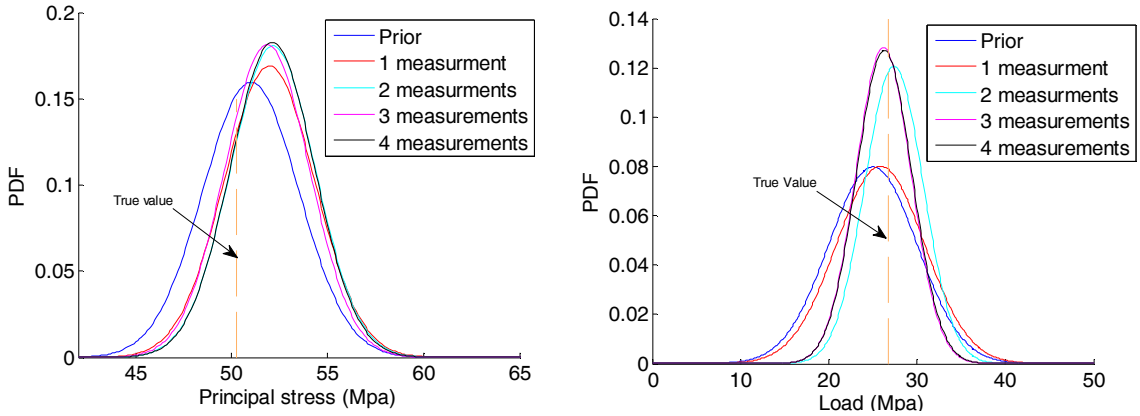

Figure 7.7 The posterior distribution of principal stress and applied load

Based on the current investigation, it can be seen that the LHS is a powerful tool for efficient large dimensional experiment design. With the help of the developed surrogate model, it will be more efficient for probabilistic analysis using Monte Carlo-based methods. The uncertainties of each model parameter can be gradually reduced using Bayesian updating when more and more measurements are available.

As a summary, the technical achievements mainly include the numerical simulation using XFEM and CZM methods and probabilistic prognosis based on the Bayesian updating technique.

CHAPTER 8 EDUCATIONAL ACHIEVEMENTS

US DOT/PHMSA sponsored CAAP program at the University of Colorado-Denver (CU-Denver) facilitates unique team collaboration between professors, graduate and undergraduate research students and leading engineers in industry to develop technological solutions that address unmet pipeline safety needs, as well as to attract and train the young generation of researchers/engineers across the pipeline field. An innovative "Team-Approach" research model was developed and implemented at CU-Denver Engineering thanks to the continued funding support from the CAAP since 2013. With the close collaborations between CU, pipeline industry and federal agency (US DOT), this new research, educational and interaction model of connecting different level of students, researchers and engineers with various backgrounds were successfully built in the past two years. The PI's model of integrating the pipeline safety research, educational and outreach goals within the CAAP frame is shown in Figure 8.1 which includes five key components: (1) unmet pipeline safety needs; (2) engineering (sensor technology, material, chemical, electronic and software technology); (3) market; (4) regulations (US DOT) and (5) innovative solutions.

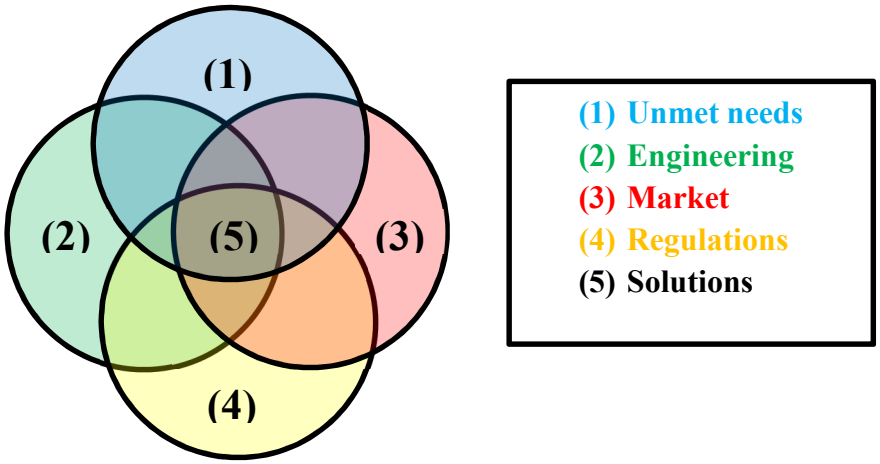

Figure 8.1 Integration of pipeline safety research, educational goals in CAAP "Team-Approach" Model

A university team of one professor PI (Deng) and over ten student researchers who have been fully or partially supported by CAAP13 and CAAP14 is working with several pipeline industry teams and trying to bring innovations to market. This "Team-Approach" model aims to connect cutting edge and fundamental research with end-user challenges identified by industry partners through this CAAP program. With the continued sponsorship of CAAP, PhD student (CAAP13), Mia Chen visited the world-class facilities of Gas Technology Institute in Chicago and interacted with researchers, regulators and operators during her USDOT R&D Forum trip in August 2014. She now becomes a senior team leader in both CAAP13 and CAAP14 projects at CU. CAAP PhD students Salem Egdaire and Mia Chen won the prestigious American Society for Nondestructive Testing Student Awards two years in a row (2014 and 2015) and presented their research findings at the ASNT annual research symposium. Currently, the vibrant CAAP team at CU has three PhD students and five MS students whose expertise span from piping materials loss diagnosis, electromagnetic, optical and acoustic sensors development, numerical modeling and data analytics for early detection of pipeline damage. The students are well exposed to industry needs, which will not only help to disseminate the knowledge developed in CAAP research to a larger group of researchers in this field, but also benefit industry partners through early stage technology development and university outreach program. The PI takes advantage of this unique "Team-Approach" and educates students at undergraduate, MS and PhD levels with different design, development, marketing and intellectual property trainings. For example, university-industry meetings and technology demonstrations between CU CAAP team, EchoRFID and ProStar were succuessfully held in 2015. CAAP students are anticipated to work on real world projects as a team to address pipeline safety challenges in both laboratory and field environment. Through the continued support from CAAP, the PI will leverage the existing and successful program at CU, attract more students with the hope of illustrating how their highly desired engineering discipline can be translated into the pipeline field. Current CAAP students at the CU-Denver have shown great interests to pursue career opportunities in the pipeline industry. As a university researcher and educator, the PI has witnessed the early success of CAAP program and the tremendous impacts of the program brought to the academia and industry.

Arizona State University has implemented a hierarchical student team structure to have different levels of research and training activities among PhD, MS, and undergraduate students. The PhD level students are usually fully sponsored by the project and focus on the more challenging and theoretical developments. The MS level students are usually partially sponsored by the project and focus on the experimental testing and demonstration studies. The undergraduate level students are usually co-sponsored by the ASU internal programs and the CAAP project and focus on the basic skill training and experimental data analysis. This student team structure ensure the proper use of the CAAP funding to deliver the required outcomes in a timely manner and significantly enhance the broad impact of the CAAP funding by involving multiple level of students and funding sources. The student team members are working closely to maximum the interaction from each individual components to achieve the overall technical objectives. For example, PhD student (Peng) is working for the CAAP 13 and 14 projects and is developing the new Bayesian information fusion framework. MS students (Sahil, Vishal, and Varun) are working on the different components for finite element simulation and experimental testing. The undergraduate student (Andrew) is co-sponsored by the ASU FURI (Fulton Undergraduate Research Initiatives) and is working closely with the MS students (Varun and Vishal) for the training and application of basic FEM simulation skills and experimental testing techniques. The pictures below show that Andrew was conducting experiments in the lab and these pictures have been shown in the 2015 FURI research symposium at ASU.

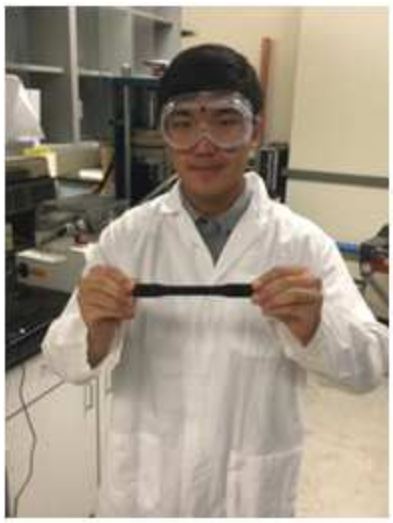

Figure 8.2 Undergraduate student Andrew was conducting experimental testing for PA 11

The PI (Liu) at ASU thought that continued CAAP funding and the developed hierarchical student team structure are really important for the education and training of next generation pipeline engineers in the future. The education and research activities for the pipe safety in the existing engineering programs (e.g., mechanical engineering or material engineering) are much lower compared to some other topics. In order to attract more engineering students and prepare them better for the future jobs in pipeline industry, integrated research and educational activities are essential to maintain the critical mass for both faculties and students in this area. At ASU, the continued CAAP support and student involvement already showed impact on students. Many students have expressed their strong interest to be part of the project. Thus, CAAP project does not only offer excellent research opportunities for future technology development, but also open the door for the wider dissemination of knowledge to future engineers as a long term goal.

REFERENCES CITED

1. Mamoun, M.M., J.K. Maupin, and M.J. Miller, *Plastic Pipe Failure, Risk and Threat Analysis.* Gas Technology Institute, 2009: p. 313.
2. Siegmund, T., *A numerical study of transient fatigue crack growth by use of an irreversible cohesive zone model.* Int. J. Fatigue, 2004. **26**(9): p. 929-939.
3. Bouvard, J.L., et al., *A cohesive zone model for fatigue and creep–fatigue crack growth in single crystal superalloys.* International Journal of Fatigue, 2009. **31**(5): p. 868-879.
4. Fawaz, S.A., *Application of the virtual crack closure technique to calculate stress intensity factors for through cracks with an elliptical crack front.* Engineering Fracture Mechanics, 1998. **59**(3): p. 327-342.
5. Servetti, G. and X. Zhang, *Predicting fatigue crack growth rate in a welded butt joint: The role of effective R ratio in accounting for residual stress effect.* Engineering Fracture Mechanics, 2009. **76**(11): p. 1589-1602.
6. Giner, E., et al., *An Abaqus implementation of the extended finite element method.* Engineering Fracture Mechanics, 2009. **76**(3): p. 347-368.
7. Sukumar, N., et al., *Partition of unity enrichment for bimaterial interface cracks.* Int. J. Numer. Meth. Engng., 2004. **59**: p. 1075-1102.

8. Razavi-Nouri, M., *Creep and stress relaxation behavior of polypropylene, metallocene-prepared polyethylene and their blends.* Iran. J. Chem. Eng, 2012. **9**: p. 60-68.
9. Osswald, T., *Understanding Polymer Processing.* Editorial Hanser, USA, 2011: p. 22-23.
10. McKenna, G.B., *On the physics required for prediction of long term performance of polymers and their composites.* NIST Journal of Research, 1994. **99**: p. 169-189.
11 http://www.me.umn.edu/labs/composites/Projects/Polymer%20Heat%20Exchanger/Creep%20description.pdf.
12. Meyers, M.A. and K.K. Chawla, *Mechanical behavior of materials.* Cambridge university press, Cambridge, 2009. **2**.
13. Hay, A., et al., *Reduced-order models for parameter dependent geometries based on shape sensitivity analysis.* Journal of Computational Physics, 2010. **229**(4): p. 1327-1352.
14. Hay, A., J. Borggaard, and D. Pelletier, *Improved low-order modelling from sensitivity analysis of the proper orthogonal decomposition.* Journal of Fluid Mechanics, 2009. **629**: p. 41-72.
15. Box, G.E.P. and N.R. Draper, *Empirical Model Building and Response Surfaces.* John Wiley & Sons, New York, NY, 1987.
16. Myers, R.H. and D.C. Montgomery, *Response surface methodology:process and product optimization using designed experiments.* Wiley, New York, 1995.
17. McKay, M.D., R.J. Beckman, and W.J. Conover, *A Comparison of Three Methods for Selecting Values of Input Variables in the Analysis of Output from a Computer Code.* Technometrics (American Statistical Association), 1979. **21**(2): p. 239-245.
18. Audze, P. and V. Eglajs, *New approach for planning out of experiments.* Problems of Dynamics and Strengths, 1977. **35**: p. 104-107.
19. Park, J.S., *Optimal Latin-hypercube designs for computer experiments.* Journal of Statistical Planning and Inference, 1994. **39**: p. 95-111.
20. Ye, K.Q. and W. Li, *Algorithmic construction of optimal symmetric Latin hypercube designs.* Journal of Statistical Planning and Inference, 2000. **90**(145-159).
21. Jin, R., W. Chen, and A. Sudjianto, *An efficient algorithm for constructing optimal design of computer experiments.* Journal of Statistical Planning and Inference, 2005. **134**(268-287).
22. Adam, M.T., *G104-A2L Guide for estimation of measurement uncertainty in testing.* American Association of Laboratory Accreditation Manual, 2002: p. 10-18.
23. Bell, S., *A Beginner's Guide to Uncertainty of Measurement.* The National Physical Laboratory, 2001. **2**: p. 9-16.
24. Cowles, M.K. and B.P. Carlin, *Markov Chain Monte Carlo Convergence Diagnostics: A Comparative Review.* Journal of the American Statistical Association, 1996. **91**(434).
25. Fort, G., E. Moulines, and P. Priouret, *Convergence of adaptive and interacting Markov chain Monte Carlo algorithms.* Annals of Statistics, 2012. **39**(6): p. 3262-3289.

26. Hasting, W.K., *Monte Carlo sampling methods using Markov Chain and their applications.* Biometrika, 1970. **57**: p. 97-109.
27. Peskun, P.H., *Aptimum Monte Carlo sampling using Markov chains.* Biometrika, 1973. **57**: p. 97-109.